Texas A&M University
Mechanical Engineering Department
Turbomachinery Laboratory
Tribology Group

Effect of Side Feed Pressurization on the Performance of Shimmed Foil Gas Bearings - Part II: Model, Predictions and Comparisons to Rotordynamic Measurements

Research Progress Report to the TAMU Turbomachinery Research Consortium

TRC-B&C-3-07

by

Tae Ho Kim

Research Assistant

Luis San Andrés

Mast-Childs Professor

Principal Investigator

May, 11, 2007

This material is based upon work supported by the National Science Foundation under Grant No. 0322925

Gas Foil Bearings for Oil-Free Rotating Machinery – Analysis Anchored to Experiments
NSF Funded Project, TEES # 32525/53900/ME

EXECUTIVE SUMMARY

Oil-free micro turbomachinery implementing gas foil bearings (*GFBs*) has improved mechanical efficiency and reliability. Adequate thermal management for operation in high temperature environments is an issue of importance in applications such as in gas turbines and turbochargers. *GFBs* often need a cooling gas flow, axially fed through one end of the bearings, to transport the heat conducted from a hot turbine, for example. Side gas pressurization has also a paramount effect on reducing amplitudes of motion, synchronous and subsynchronous. In a comparison 2007 TRC report, shaft motion measurements in a test rotor supported on *GFBs* show this remarkable effect.

A computational gas film model implementing the evolution of gas circumferential velocity as a function of the imposed side pressure is advanced. For tested *GFBs,* predicted direct stiffnesses and damping coefficients increase as the magnitude of feed pressure raises, while the difference in cross-coupled stiffnesses, directly related to rotor-bearing system stability, decreases. Predictions of threshold speed of instability and whirl frequency ratio are in close agreement with laboratory measurements.

A model for GFBs with shims is introduced. The shimmed GFB, whose film clearance resembles a three lobe bearing, generates significantly larger hydrodynamic pressures than those in a conventional GFB. Shimmed GFBs operate with a smaller journal eccentricity and attitude angle than conventional GFB, and with increased direct stiffness and damping coefficients.

A linear finite element rotordynamic analysis (XLTRC^2) models the test rotor supported on GFBs and predicts the system rotordynamic stability and synchronous rotor responses, phase angle and amplitude. Predicted synchronous responses are in very good agreement with the test measurements, in particular for small to moderate imbalances.

As a final observation, although external pressurization aids to improve GFB rotordynamic performance; a too large supplied gas flow rate for cooling an actual high temperature application may penalize sensibly the efficiency and performance of the turbomachinery.

TABLE OF CONTENTS

LIST OF TABLES

LIST OF FIGURES

NOMENCLATURE

$C_{\alpha\beta}$	Bearing damping coefficients; $_{\alpha\beta=X,Y}$ [N·s/m]
C_{eff}	Effective damping coefficient[N·s/m]
c	Bearing radial clearance [m]
c_{DE} , c_{FE}	Nominal radial clearance for the drive and free end GFBs, respectively [m]
c_J	Journal radial travel [m]
DV, DH	Drive end bearing, vertical and horizontal planes
e_X,e_Y	Journal eccentricity components [m], $e = \sqrt{e_X^2 + e_Y^2}$
FV, FH	Free end bearing, vertical and horizontal planes
g	Gravity
h	Film thickness [m]
$K_{\alpha\beta}$	Bearing stiffness coefficients; $_{\alpha\beta=X,Y}$ [N·s/m]
K_{eff}	Effective stiffness coefficient [N/m]
L	Bearing axial length [m]
M	Fraction of the rotor mass that each bearing supports [kg]
m_e	Mass imbalance [mg]
$\dot{m}_z$	axial flow rate through the film [m3/s]
N_{os}	Onset speed of subsynchronous motion [rpm]
P	Hydrodynamic gas pressure [N/m^2]
P_a	Ambient pressure [N/m^2]
P_s	Side feed gas pressure [N/m^2]
P_{sub}	Gas pressure in outer gap [N/m^2]
r	Radius for imbalance mass [m]

R_J	Journal radius [m]
$\Re$	Ideal gas constant [J/Kg-K]
T	Temperature [K]
u	m_e *r/M.* Imbalance displacement [μm]
u_c	Mean circumferential flow velocity [m/s]
X, Y	Vertical and horizontal rotor displacements
x,z	Coordinate system on plane of bearing [m]
w_d	Top foil deflection [m]
WFR	Whirl frequency ratio [-]
α	Inlet flow pre-swirl factor
μ	Gas viscosity [Pa-s]
γ	Structural loss factor [-]
Θ	Bearing angular coordinate [rad]
$\Re$	Ideal gas constant [J/Kg-K]
ς	Damping ratio [-]
Ω	Rotor angular speed [rad/s]
ω_{cr}	Critical speed [rad/s]
ω_d	Damped natural frequency of the rotor-GFB system [rad/s]
ω_n	Natural frequency of the rotor-GFB system [rad/s]

Subscripts

α, β	Directions of perturbation for first order pressure fields (*X*, *Y*)
l, t, p	Pad leading and trailing edges, and offset position

I. INTRODUCTION

Reliable high speed operation of gas foil bearings (GFBs) ensures high efficiency in turbomachinery and lessens maintenance requirements [1]. Comprehensive modeling of GFBs anchored to relevant test data will enable the widespread usage of GFBs into novel turbomachinery applications, such as hybrid fuel cell-turbine power systems and micro-engines recharging battery packs for clean hybrid electric vehicles [2,3]. GFBs are often supplied with a cooling gas flow for high speed and high temperature operation [4]. Side pressurization in a GFB forces a cooling gas flow, axially fed through one end of the bearing, thus preventing hot-spots in the shaft and bearing, and extending their life.

Side gas pressurization, however, also affects the rotordynamic performance of GFBs, i.e. it delays the onset speed of subsynchronous rotor motions and reduces subsynchronous peak amplitudes as shown in the companion report [5]. The report [5] also demonstrates that installing shims in GFBs increases the natural frequency of the test rotor-GFB system, thus delaying the threshold speed of instability where amplitude of large subsynchronous motions suddenly appear. Normalization of the synchronous rotor amplitudes verifies the linearity of the rotor – GFB system response within the test speed range (max. 50 krpm).

This report presents a physical model for prediction of the forced performance of GFBs supplied with side feed gas pressurization. The gas film model includes the evolution of gas circumferential velocity as a function of the imposed side pressure. The gas film equation for hydrodynamic pressure generation is coupled to the FE structural model developed in [6]. A simple stability analysis [7] gives the rotordynamic characteristics of the test GFB with side pressurization. The predicted threshold speed of instability is in close agreement with test measurements.

A model for GFBs with machined mechanical preload introduced in 2006 TRC report [8] is modified to predict the performance of shimmed GFBs. A sinusoidal function approximately depicts the assembly radial clearance modified due to installation of three shims. The shimmed GFB generates significant hydrodynamic pressures with peaks at the three shim locations, while the original GFB shows much lower film pressures. Installation of shims into the GFBs leads to an increase in direct stiffness and damping coefficients. Changes in cross-coupled force coefficients are relatively small.

A linear finite element rotordynamic analysis (XLTRC2®) models the test rotor supported on GFBs and predicts the system rotordynamic stability and synchronous rotor responses. The predicted amplitude and phase angle of the synchronous responses show good agreement with the test measurements recorded during rotor coastdown tests with small to moderate imbalance masses.

II. LITERATURE REVIEW

Modeling and performance prediction of micro turbomachinery with a rotor supported on GFBs requires accurate performance predictions of GFBs anchored to reliable test data. Heshmat et al. [9,10] introduce the first analyses of bump type GFBs, coupling the gas film hydrodynamic pressure to a simple elastic foundation model and neglecting the top foil. Since then, Carpino and Talmage [11,12], San Andrés and Kim [6], and Lee et al. [13] advance predictive *GFB* models including a shell FE description of the top foil and a distributed elastic support structure.

To date, Carpino and Talmage [11,12] have advanced the most complete computational models, including detailed descriptions of membrane and bending effects of the top foil, and accounting for the sub-foil structure elastic deformation. The authors introduce a fully coupled FE formulation, with membrane and bending stresses in a cylindrical shell coupled through moment, tension, curvature, and strain expressions. The model incorporates both the pressure developed by the gas film flow and the structural deflections of the top and bump foils into a single finite element. The predictions exhibit irregular shapes of pressure and film thickness due to foil detachment in the exit region of the gas film. In Ref. [12], a simple elastic foundation model for the structural bump layer [11] is improved as a continuous elastic foundation which accounts for the radial and circumferential deflections of the bumps, but does not show the typical sagging effect of the top foil between adjacent bumps. In the model, one half of a symmetric bump is analyzed while ignoring the curvature of the bump strip layer. The energy dissipation is calculated using an equivalent viscous damping model for dry-frictional effects between the top foil and bumps, and between the bumps and the bearing housing. The effects of whirl orbit amplitude and frequency and dry-friction parameters on predicted bearing stiffness and damping coefficients are studied for a low load application (specific pressure of 1.36 bar [19.7 psi]).According to the authors' predictions, the direct damping coefficients decrease as the

dry-friction coefficient increases because there is stick of the bumps against the bearing, for example. These results are in opposition to those in [14]; however, the physical phenomenon is different, i.e. direct damping coefficients increase with an increasing dry-friction coefficient. None of the references of Carpino and co-workers listed above includes comparisons to actual GFB experimental data and; in all cases, predictions advanced refer to Generation I GFBs only.

San Andrés and Kim [6] model the top foil as a structural shell and integrate it with the bump strip layers in conjunction with the hydrodynamic gas film to predict the static and dynamic load performance of GFBs. Ref. [8] details two FE models for the top foil supported on bump strips, one is a 2D shell anisotropic structure and the other a 1D beam-like structure. The Cholesky decomposition of the global stiffness matrix for the top foil and bump strips is performed off-line prior to computations coupling it to the gas film analysis governed by Reynolds equation. The procedure greatly enhances the computational efficiency of the numerical scheme. Predictions of journal attitude angle and minimum film thickness for increasing static loads and two journal speeds are obtained for a GFB tested by Ruscitto et al. [15] [1]. 2D FE model predictions slightly overestimate the minimum film thickness at the bearing centerline, while underestimating it at the bearing edges. Predictions from the 1D FE model compare best to the available tests data; reproducing closely the measured circumferential wavy-like minimum film thickness profile. This prediction evidences the local deformation of the top foil as well. The 1D top foil model is recommended due to its low computational cost. Predicted stiffness and damping force coefficients versus excitation frequency show the two FE top foil structural models result in slightly lower direct stiffness and damping coefficients than those from the simple elastic foundation model [16].

Lee et al. [13] also advance a computational model integrating the foil sub-structure. The FE models for the top foil and bump strip layer are coupled to gas film pressure hydrodynamic model and predicts the bearing minimum film thickness, attitude angle, and force coefficients. The authors also conduct experiments to identify frequency-independent stiffness and damping coefficients of a test floating GFB from measurements of an applied impact load and ensuing bearing motions (impedance formulation). Predicted direct stiffnesses agree reasonably with test

[1] This publication is the only one in the open US literature with enough technical information to allow predictive models to calibrate predictions for a first-generation GFB. The literature on commercial applications of GFBs is extensive. However, relevant technical information is scant, and at times even misleading. There are no archival publications which fully detail the geometry of 2nd and 3rd generation type GFBs, for example.

data for operation between 15 to 25 krpm; while predicted and test-derived damping coefficients decrease as rotor speed increases. Unfortunately, this publication does not provide enough information on the bearing tested (geometry, materials, etc) and, in the authors' point of view, implements an identification method not appropriate for GFBs.

Heshmat et al. [17] predict the static load performance of thrust GFBs. The numerical procedure couples a finite element model of the structural supports, generated by a commercial code, to the gas film hydrodynamics modeled with finite differences. Shells model the top foils, which are supported on a simple elastic foundation representing the bump strips. Comparison of predicted static load capacity to measurements shows good agreement. Heshmat et al. [18] predict the static performance of radial GFBs to investigate the feasibility of a hybrid foil–magnetic bearing configuration. The numerical model in [17] is enhanced by efficiently using a structural influence coefficient matrix representing the combined action of top foil and bumps.

A gas foil bearing has an ultimate load capacity at a journal eccentricity well in excess of its *nominal* bearing clearance. In actuality, the *nominal* clearance in a GFB is a vague concept. Peng and Khonsari [19] introduce a unique analysis for the ultimate load capacity of GFBs at *infinite* speed number operation. A bearing clearance and underlying stiffness of the foil support determine this load. In practice, however, either by design or due to inaccurate manufacturing, GFBs do not posses an actual clearance, i.e. an *air gap* between the journal and its support structure. For mechanical integrity, GFBs are usually preloaded (assembly interference or shimmed), with the journal diameter being larger than that of the top foil. The preload ensures even contact at the static condition (no shaft speed) with uniform pressures pushing on the elastic structure. Radil et al. [20] find a strong correlation of GFB measured load capacity to the assembly clearance. In operation, the journal grows due to thermal and centrifugal effects, thus exacerbating the effects of the largely unknown GFB "clearance."

Kim and San Andrés [21] retake the analysis in [19], include the effect of an assembly preload, and provide analytical formulae for estimation of load capacity, minimum film thickness and stiffness coefficients for operation at large shaft speeds, *infinite* in theory. The underlying elastic structure (bump foil strip) determines the ultimate load capacity of a GFB as well as its stiffnesses, along with the limiting journal displacement and structural deformation. Thus, an accurate estimation of the actual *minimum film thickness* is found prior to performing calculations with a complex computational model, even for the case of large loads that result in a

journal eccentricity well exceeding the nominal clearance, if applicable. An initial assembly preload (interference between shaft and foil) increases the GFB static stiffness at both null and infinite rotor speeds. Predictions reproduce with exactness measured structural stiffness and elastic deformation for the contact condition between shaft and foil, i.e. without journal rotation.

Pressurized feed air is often needed to cool GFBs as well as the integral drive motor (or generator) mounted between GFBs in oil-free rotating machinery, for example [22]. However, for sufficiently high pressures, the side gas flow will affect the rotordynamic performance of GFBs. Measurements in [23] demonstrate that the external air pressurization through a bearing end not only reduces the amplitude of synchronous motions while crossing a critical speed, but ameliorates the amplitudes of subsynchronous motion for operation at shaft speeds about two times the critical speed.

The effect of side pressurization on GFB force performance may be derived from similitude to annular pressure seals, for example. Allaire et al. [24] analyze short length annular liquid seals, $L/D = 0.16$, considering the circumferential flow is relatively small relative to the axial flow. Thus, a circumferential momentum equation is not considered in the analysis, i.e. the continuity and axial momentum equations are used to evaluate the seal forced performance. Pressure boundary conditions are determined by considering a Bernoulli type non-isentropic head loss. Perturbed pressures, axial flow velocity, and film thickness about a rotor equilibrium position determine the stiffness and damping coefficients as well as the load capacity of short seals. The model predictions show that short seals produce large stiffness and damping coefficients; and due to the slow development of circumferential flow, small cross-coupled stiffness coefficients. In general, the whirl frequency ratio, an indicator of bearing stability, equals the inlet swirl ratio in short length seals [25].

Black et al. [26] present the effects of fluid inlet swirl velocity on the force performance of annular liquid seals. Prior models incorrectly assume a fully developed circumferential flow over the whole seal axial length. Black et al., on the other hand, show that the circumferential velocity approaches one half of rotor surface speed as the seal axial length increases. Model predictions note that the proper amount of anti-swirl inlet velocity strongly reduces or even eliminates seal cross-coupled stiffness coefficients.

Adequate thermal management is necessary when incorporating GFBs into high temperature applications, such as in a gas turbine engine [27]. A side cooling flow aids to prevent GFBs from

encountering thermal seizure, thus maintaining an adequate load capacity and stability [26]. Salehi et al. [28] predict GFB static load performance and temperature fields by using Reynolds and gas film energy transport equations coupled to the *simple elastic foundation model* [9]. The Couette flow approximation [29] simplifies the energy equation by neglecting the work done by pressure, and effectively uncouples it from the Reynolds equation. Thus, the analysis calculates only the circumferential temperature distribution at the bearing mid-plane. The axial temperature distribution is assumed to linearly decrease toward the bearing edges. Experiments aid to estimate the temperature-raise of the cooling flow passing through the GFB by measuring the flow inlet and outlet temperatures using thermocouples installed on the outer side of the top foil. The measurements reveal that the GFB has a greater temperature along the static load direction rather than in the opposite direction. The temperature grows with increasing rotor speeds and static loads. A comparison of the predicted temperature-rise of the cooling flow to the experimental measurement shows good agreement within a deviation of ~20 %.

Peng and Khonsari [30] introduce a THD model to predict the steady-state performance of GFBs. A simple elastic foundation represents the foil structure with coupled Reynolds and thermal energy transport equations solved simultaneously for prediction of the gas film pressure and temperature fields. Heat convection coefficients based on the cooling flow regime are obtained. Predictions reveal a nearly uniform film temperature along the bearing axial direction; and with an increase in load capacity since typical gas viscosity increases with temperature. Comparison of predicted temperatures to test data in [27] is noted as excellent. However, Radil and Zeszotek [31] find a decrease of ~30 % in load capacity for a GFB tested at increasing temperatures ranging from 25ºC to 650 ºC. Apparently, temperature dependent mechanical properties of the structural components and actual dimensions (thermal growth) need be accounted for reliable predictions.

Fluid film journal bearings often incorporate a machined mechanical preload to enhance the hydrodynamic wedge that generates the pressure field able to produce a centering stiffness. The preload can be given to a GFB with either a varying bump strip height, or a machined radial preload, or by inserting metal shims underneath a bump strip layer and in contact with the bearing cartridge [32,33]. Kim [34] extends the computational model developed in [6] to predict the performance of shimmed GFBs. The inner profile of the GFB is generated by considering the location, length, and thickness of three shims leading to a three lobe-like bearing. The model

predictions show hydrodynamic pressures even without a static load, i.e., rotor centered operation, and increased direct stiffness and damping force coefficients.

III. GAS FOIL BEARING WITH SIDE PRESSUZIZATION

III-1. COMPUTATIONAL MODEL

Figure 1 shows a schematic depiction of a GFB and a journal rotating with angular speed Ω. An imposed pressure differential (P_s-P_a) forces a cooling flow through the foil bearing. The graph depicts the evolution of gas velocities through the inner and outer flow regions. The inner flow, between the rotating journal and top foil, is characterized by a minute film thickness (h). The outer flow passing through the back side of the top foil has a much larger characteristic length, typically a *bump* height.

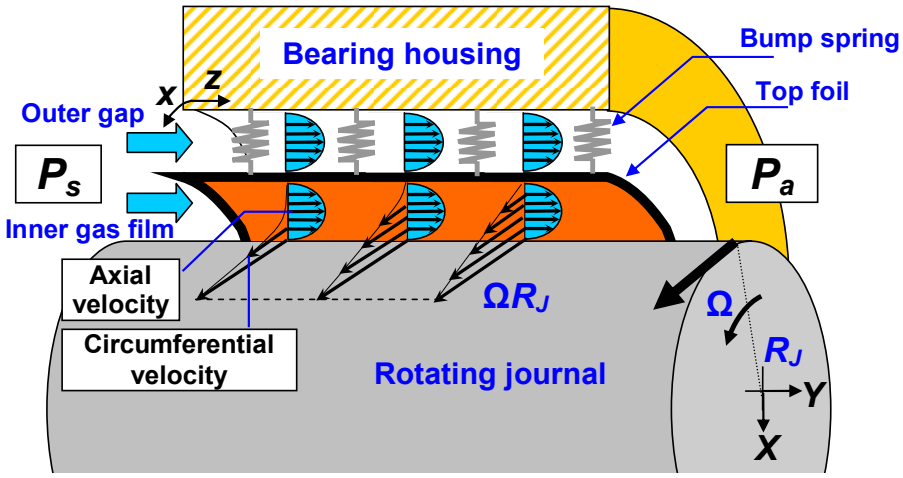

Figure 1. Flow induced by side feed pressure in a foil bearing. Schematic view of evolution of gas velocities between journal and top foil (inner film flow) and between top foil and bearing housing (outer flow).

San Andrés at al. [23] observes that the axial flow rate induced by side pressurization retards the development of the mean circumferential flow velocity (u_c) within the *GFB*, as is commonly

asserted in annular pressure seals [24,26]. For centered journal operation, the gas mean flow circumferential velocity varies along the axial coordinate z [24] as

$$u_c = \frac{\Omega R_J}{2}\left(1-e^{-\delta z}\right)+\alpha\ \Omega R_J e^{-\delta z} \tag{1}$$

where $\delta = 12\mu/(\dot{m}_z c^2)$; $\dot{m}_z = \frac{c^2}{24\,\mu\,\Re\,T}\frac{\left(P_s^{\,2}-P_a^{\,2}\right)}{L}$ (2)

$\Re$ =287 J/kg-K and viscosity μ = 1.87 ×10^{-5} Pa-s for air. $\dot{m}_z$ is the axial flow rate through the film, and α is an inlet flow pre-swirl factor, hereby taken as null since in the tests the pressurized air flow impinged directly into one bearing end, see Fig. 1. Note that as z → ∞, u_c → 0.5 ΩR_J, i.e. 50 % of rotor surface speed. The ideal isothermal and isoviscous gas film pressure *(P)* within the foil bearing is governed by an appropriately modified Reynolds equation incorporating the evolution of circumferential flow velocity,

$$\frac{\partial}{\partial x}\left(Ph^3\frac{\partial P}{\partial x}\right)+\frac{\partial}{\partial z}\left(Ph^3\frac{\partial P}{\partial z}\right)=12\mu\left[\left(1-e^{-\delta z}\right)\frac{\Omega R_J}{2}\frac{\partial(Ph)}{\partial x}+\frac{\partial(Ph)}{\partial t}\right] \tag{3}$$

in the film region {0<x=ΘR_J<2πR_J, 0<z<L}. The film thickness (h) for an aligned journal is $h=c+e_X\,cos(\Theta)+e_Y sin(\Theta)+w_d$, where ($e_X$, e_Y) are journal center displacements and w_d is the deflection field of the underlying support structure. w_d is proportional to the pressure difference {P-P_{sub}} and a function of the material, thickness and geometry of the top foil modeled with shell FEs and the underlying elastic support structure [6]. The flow of gas through the outer region behind the top foil is only axial, not greatly restricted by the bearing underspring structure.

The boundary conditions for the gas film pressure field are $P(\Theta,0)=P_s$, $P(\Theta,L)=P_a$, and $P(\Theta_\eta,z)_{\eta=l,t}=P_{sub}(z)$ at the leading (Θ_l) and trailing (Θ_t) edges of a top foil. The gas pressure behind the top foil (P_{sub}) equals:

$$P_{sub}(z)=\left[P_s^{\,2}\left(1-\frac{z}{L}\right)+P_a^{\,2}\left(\frac{z}{L}\right)\right]^{0.5} \tag{4}$$

As in Ref. [16], small amplitude journal motions about an equilibrium position render *PDEs* for the zeroth- and first- order pressure fields; and from which, prediction of the *GFB* reaction forces and force coefficients, stiffness and damping, [$K_{\alpha\beta}$, $C_{\alpha\beta}$] $_{\alpha\beta=X,Y}$, follow. The model does not

include thermal energy transport considerations since these were unimportant for the laboratory test conditions.

III-2. PREDICTED BEARING PERFORMANCE

Figure 2 introduces a layout of the TAMU rotor-GFBs test rig and instrumentation, fully described in the companion report [5]. The test rotor weighing 1 kg is supported on two GFBs, each of length and diameter equal to 38.1 mm. The test rig housing holds two test GFBs and contains an internal duct to supply air pressure up to 7 bars (100 psig). The air pressurization at rotor midspan forces a cooling flow through the test GFBs. A 0.75 kW (1 HP) electric motor with maximum speed of 50 krpm drives the test rotor through a flexible coupling. A starter motor, 1.49 kW (2.0 HP) with maximum speed of 25 krpm, aids the driving motor to start up the test rotor through a centrifugal clutch before the rotor lifts off from its bearings. See Ref. [5, 35] for a more detailed description of the test rig and bearings.

Model predictions follow for the free end GFB tested in Ref. [5]. See Table 1 for the geometry of the test GFB. For rotor operation at 30 krpm (500 Hz), Fig. 3 shows the predicted journal eccentricity and attitude angle versus side feed (gauge) pressure. As the side pressure increases, the predicted journal eccentricity increases and journal attitude angle decreases. Note that test measurements with side feed pressurization, Ref. [5], show small static rotor motions along the horizontal direction as the rotor speed increases, thus implying a reduction in cross-coupled effects. In Fig. 4, as the side pressure increases, the minimum film thickness and drag torque decrease. The axially fed gas flow due to side pressurization retards the evolution of gas velocities in the circumferential direction, thus decreasing the drag torque and minimum film thickness, and increasing the operating journal eccentricity.

Figure 5 shows predicted (a) direct (K_{XX},K_{YY}) and cross-coupled (K_{XY}-K_{YX}) stiffnesses and (b) direct (C_{XX},C_{YY}) damping coefficients versus excitation frequency at shaft speed of 30 krpm (500 Hz). Direct stiffnesses and damping coefficients grow as side pressurization increases. Most importantly the difference (K_{XY}-K_{YX}) decreases at low frequencies denoting a net gain in bearing stability. Note also that all force coefficients are strong frequency dependent functions.

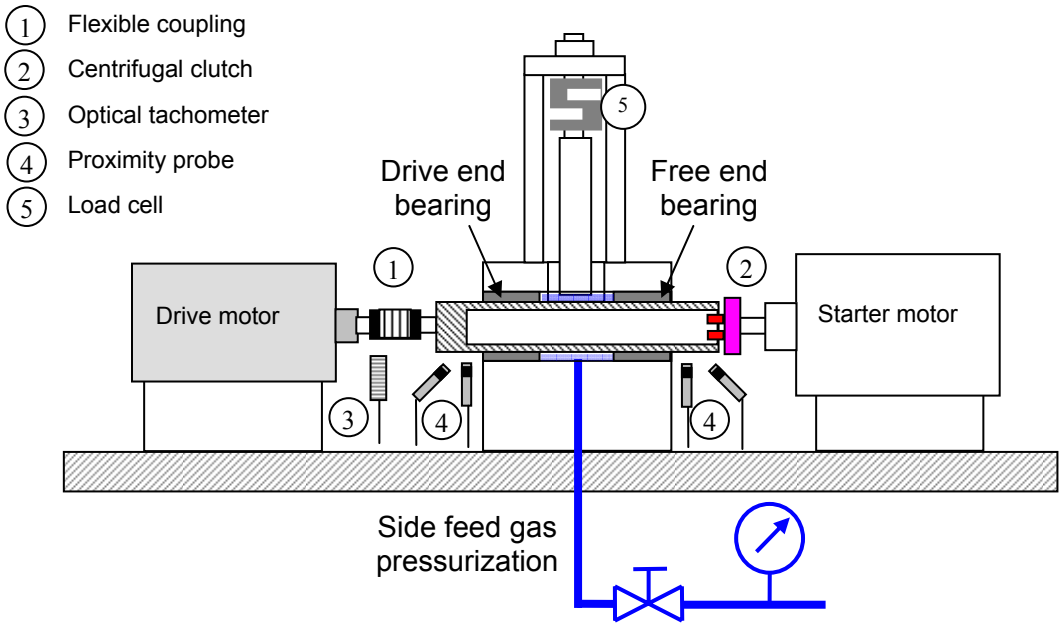

Figure 2. Layout of rotor-GFBs test rig and instrumentation

Table 1 Geometry and material properties of test GFB (free end). Static load: 4.9 N (*X*-direction).

Bearing	Radius, $R=D/2$	19.05 mm	(0.75 inch)
	Length, L	38.1 mm	(1.5 inch)
	Top foil arc circumferential length, l_x	120 mm	(4.7 inch)
	Angular distance between top foil leading edge and vertical plane, Θ_1	45 º	
	Axial length, L_s	38.1 mm	(1.5 inch)
	Estimated nominal radial clearance for free end bearing, c_{FE}	70 μm	(2.8 mil) [5]
Bump	Pitch, p	4.572 mm	(0.18 inch)
	Length, l_o	4.064 mm	(0.16 inch)
	Foil thickness, t	0.102 mm	(4.0 mil)
	Height, h	0.381 mm	(15 mil)
	Poisson's ratio, υ	0.29	
	Bump modulus of elasticity, E	213 GPa	(30.9 Mpsi)
	Dry friction coefficient, μ (estimated)	0 - 0.25 [36]	

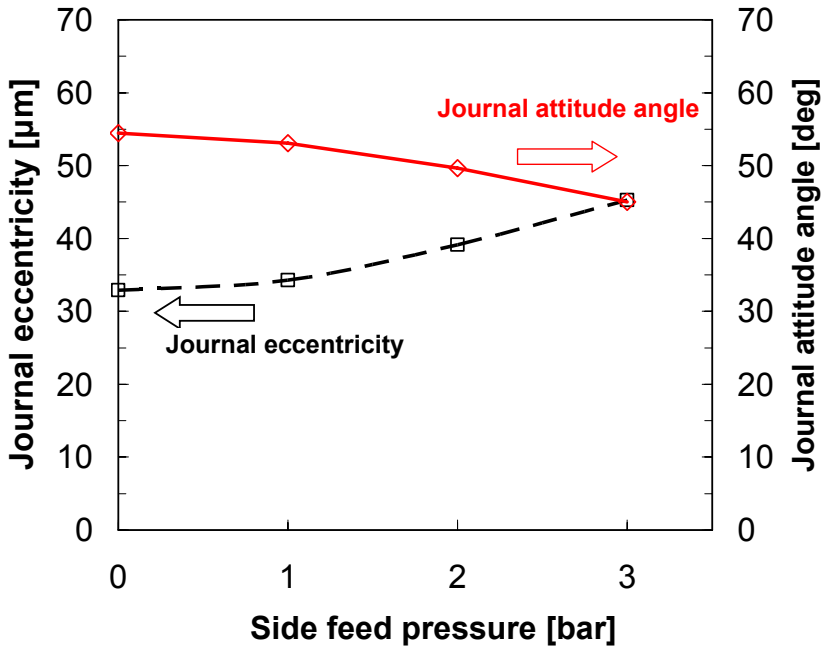

Figure 3. Predicted journal eccentricity and attitude angle versus side feed (gauge) pressure. Static load 4.9 N. Rotor speed: 30 krpm (500 Hz).

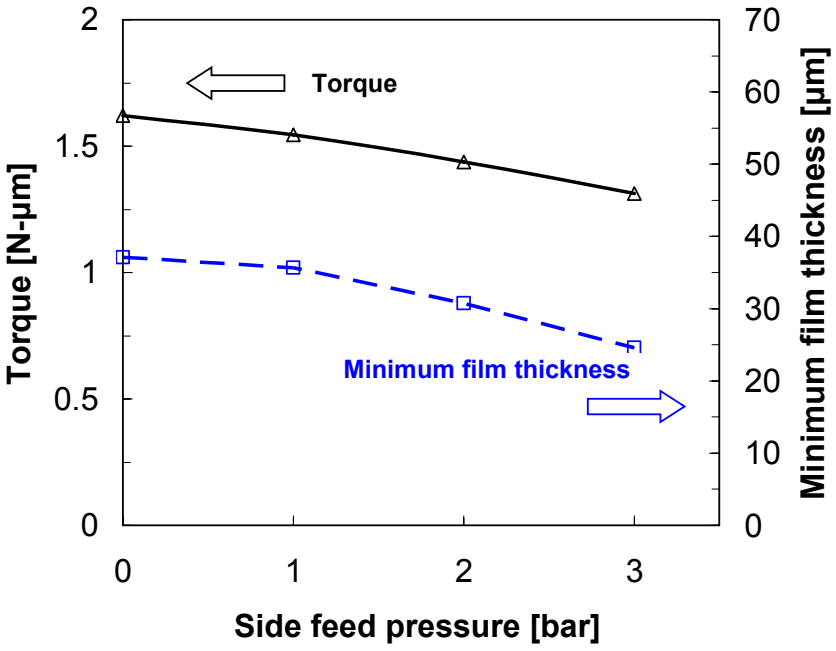

Figure 4. Predicted bearing drag torque and minimum film thickness versus side feed (gauge) pressure. Static load 4.9 N. Rotor speed: 30 krpm (500 Hz).

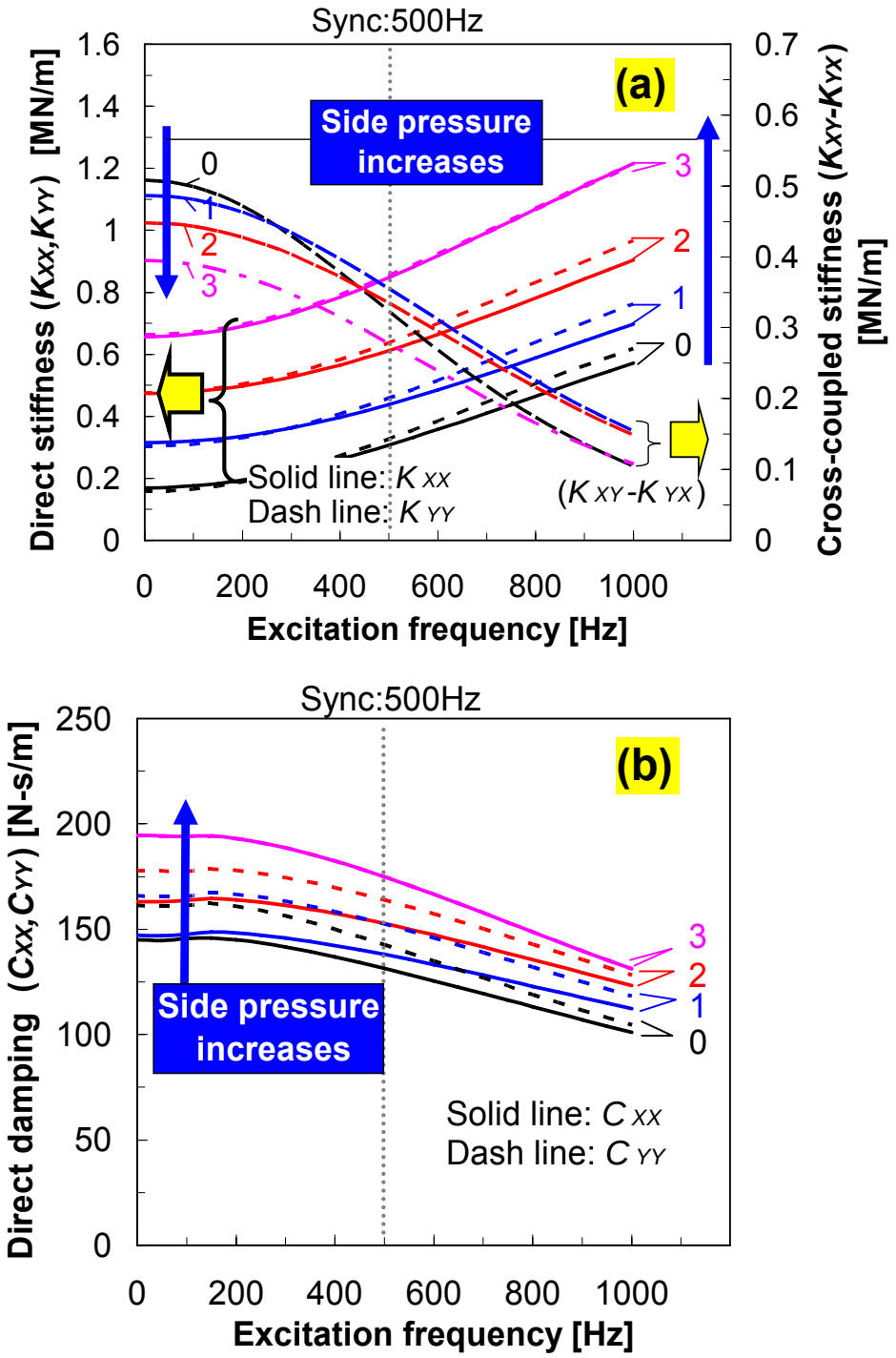

Figure 5. Effect of side pressurization on test *GFB* force coefficients. (a) Direct and cross-coupled stiffnesses (b) direct damping coefficients. Numbers denotes magnitude of side feed (gauge) pressure, P_s [bar]. Static load 4.9 N. Rotor speed: 30 krpm (500 Hz).

III-3. PREDICTIONS AND COMPARISONS TO TEST DATA

A simple eigenvalue analysis of the test rotor-*GFBs* follows Lund's approach [7] to determine stability parameters: critical mass and whirl frequency ratio (*WFR*), defined as the ratio between whirl frequency and angular shaft speed. For a shaft speed of 30 krpm and rotor ½ mass of 0.5 kg, Figure 6 shows a magnitude of side pressure, ≥ 2.9 bar, needed to ensure stable rotor operation, i.e. free of subsynchronous whirl. Note that, in Fig. 7 (i.e. see also Fig. 6 of the companion report [5]), the measured rotor subsynchronous whirl motions disappear for side feed pressures ≥ 2.8 bar, i.e. the test system becomes rotordynamically stable.

Figure 8 compares the predicted natural frequency to measured subsynchronous frequency as the side (gauge) feed pressure increases. At P_s=3 bar, the predicted whirl frequency is 165 Hz, i.e. whirl frequency ratio (*WFR*) is 0.33=165Hz/500Hz, while that determined from the measurements is 147 Hz, i.e. *WFR* is 0.29=147Hz/508Hz (see also Fig. 5 of the companion report [5]). The agreement between the predicted threshold speed of instability and the measured onset speed of subsynchronous motion in Fig. 7 taken from Ref. [5] is remarkable.

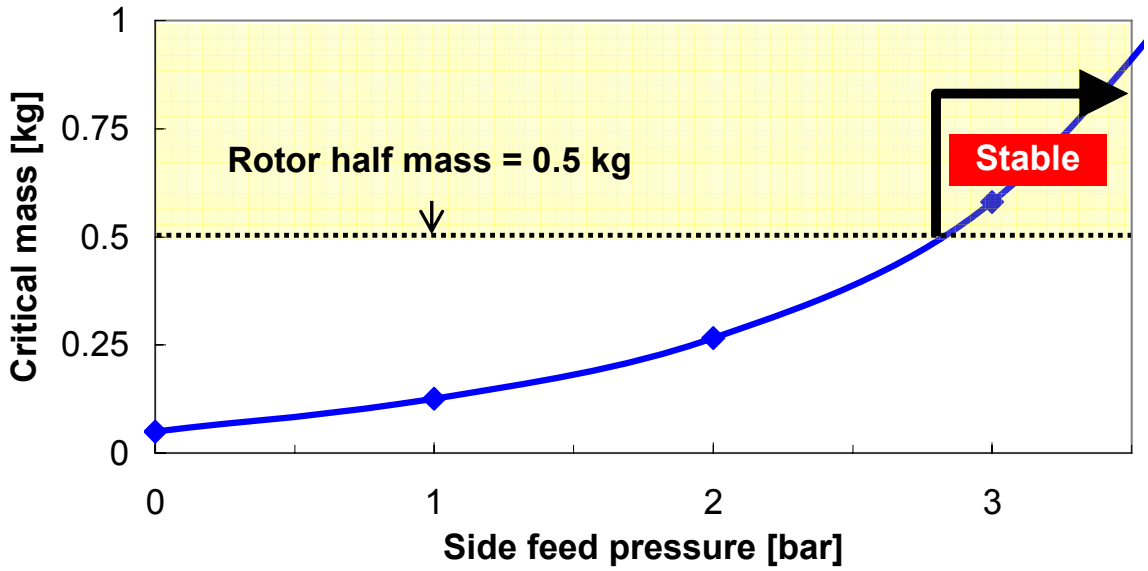

Figure 6. Predicted critical mass vs. side (gauge) feed pressure for operation of *GFB*. Static load 4.9 N. Rotor speed: 30 krpm (500 Hz).

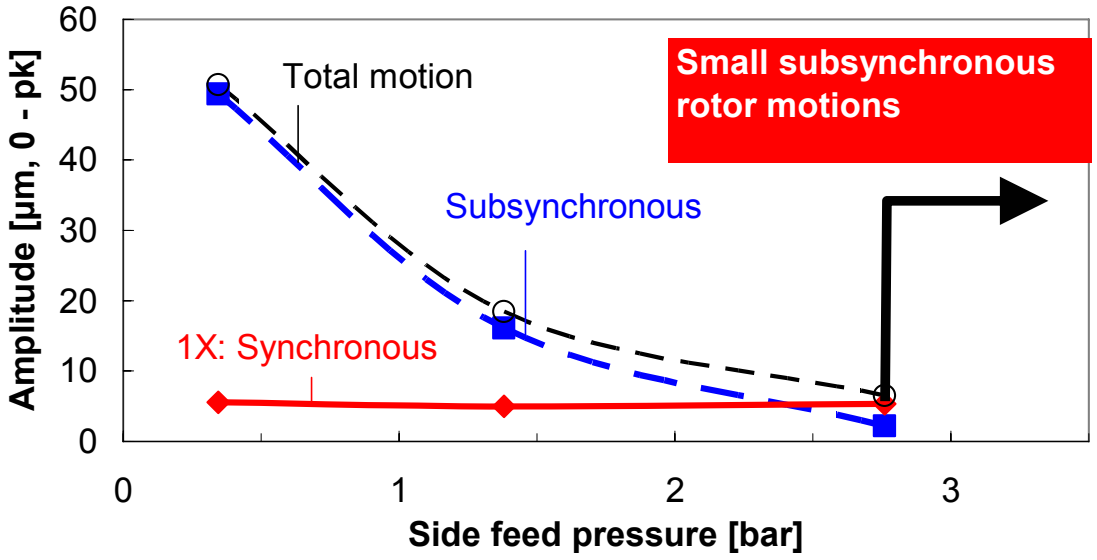

Figure 7. Amplitudes of total shaft motion, and synchronous and subsynchronous components versus side feed (gauge) pressurization. Rotor speed : 30 krpm (500 Hz) [5].

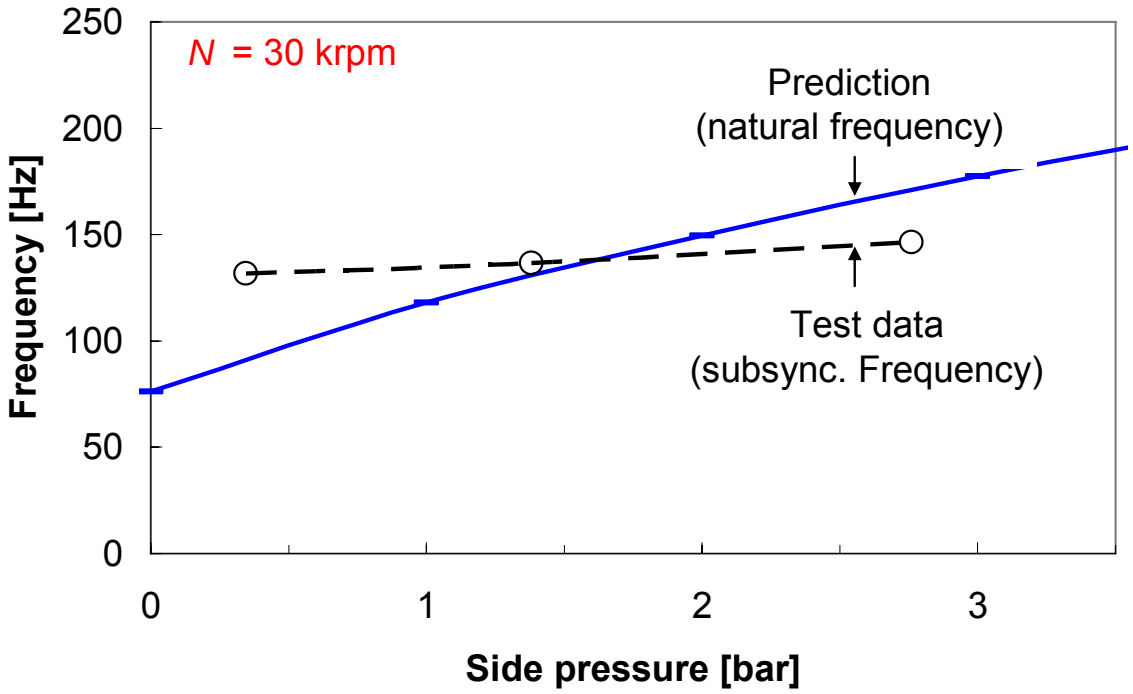

Figure 8. Predicted system natural frequency and measured subsynchronous whirl frequency versus side feed (gauge) pressure. Static load 4.9 N. Speed: 30 krpm (500 Hz).

IV. PERFORMANCE OF SHIMMED GAS FOIL BEARINGS

A 2006 TRC report [8] models a GFB with a machined preload, i.e. a GFB constructed as a "three lobe" configuration, and describes the predicted rotordynamic force performance of the GFB. The model in [8] is modified for the test GFBs with shims. A companion report [5] demonstrates that shimmed gas foil bearings delay the onset speed of large subsynchronous rotor motions during rotor speed-up (acceleration) tests. The test GFBs have three metal shims installed under a bump strip layer and in contact with the bearing cartridge at three angular locations, as shown in Fig. 9. Ref. [5] provides the geometry and material properties of the test shimmed GFBs (see also Table 1 for the geometry of the original GFBs).

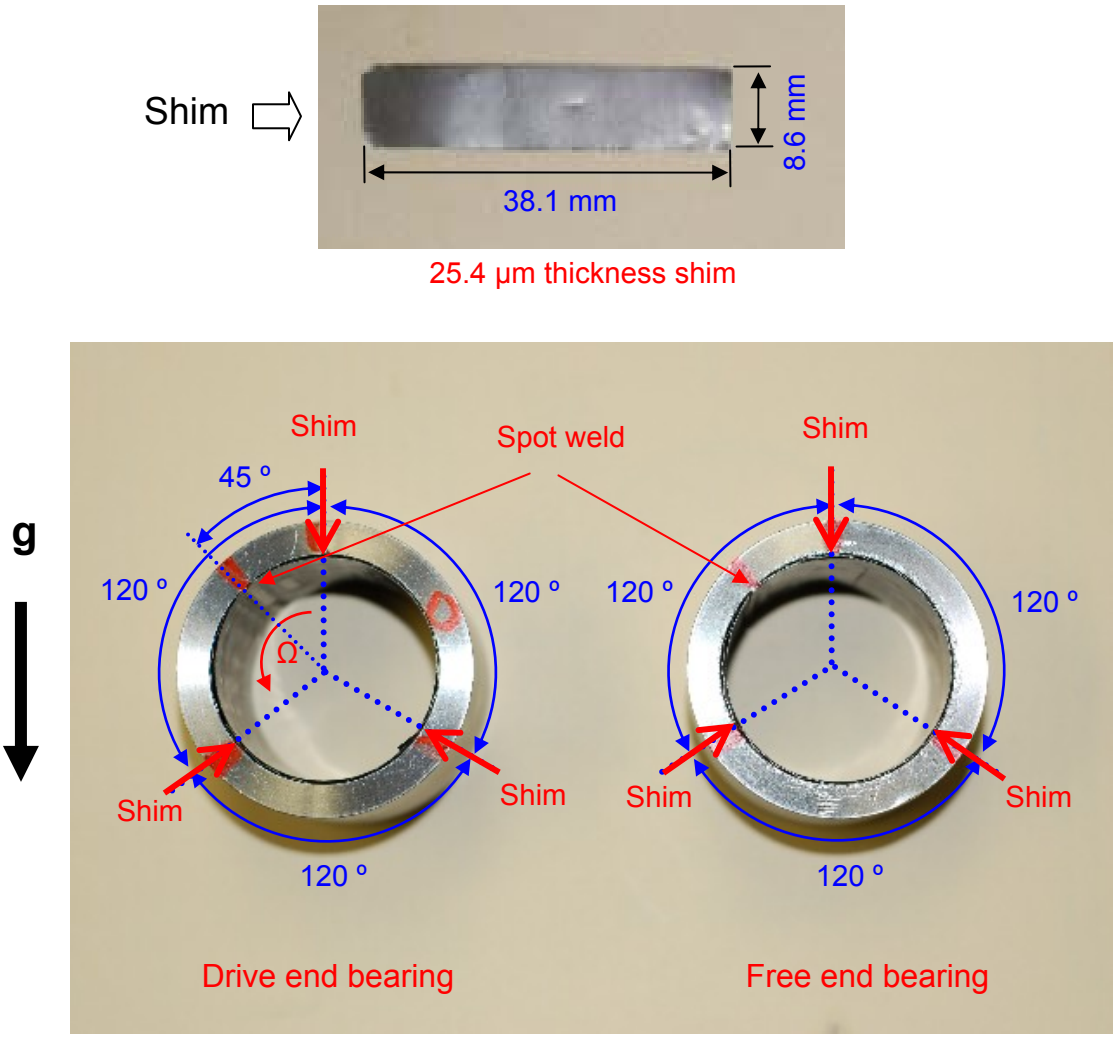

Figure 9. Locations of three shims relative to top foil spot-weld in test bearings

Figure 10 illustrates schematic views of (a) structural top foil and bump strip layer with shims, and (b) an approximation to the assembly radial clearance of the shimmed GFB for a nominal clearance of 35 μm as provided by the manufacturer[2]. Three metal shims of 25.4 μm thickness, 26 ° angular extent, and 38.1 mm length installed under the bump strip and with an angular distance, 120 ° reduce by the shim thickness the radial assembly clearance of test GFBs at three angular locations. A sinusoidal function approximately depicts the modified assembly radial clearance[3] as shown in Fig. 9.

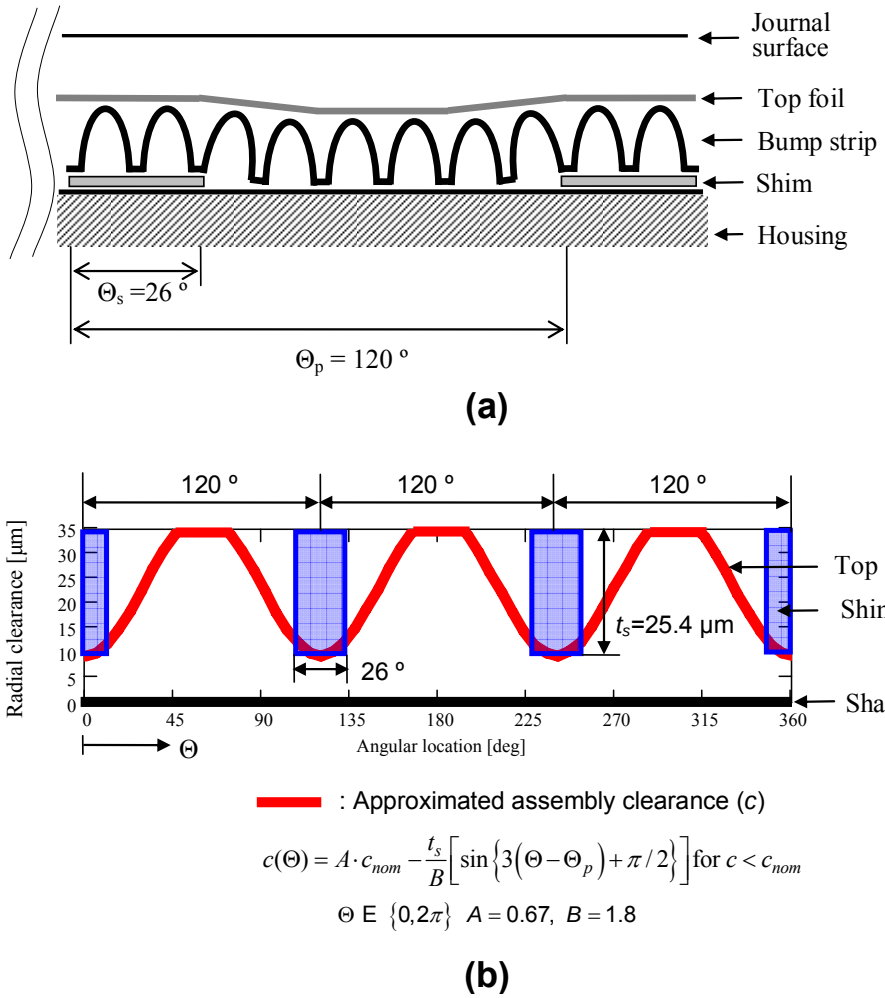

Figure 10. (a) Schematic view of a structural foil layers with shims and (b) approximation of radial assembly clearance of GFB with three shims.

[2] Radial clearances in the test GFBs are generally unknown. A load-deflection test [5] reveals the structural stiffness coefficients < 1×10^5 N/m within nominal radial clearances, c = 40 μm and 70 μm estimated for the drive and free end GFBs, respectively. Thus, the GFBs have an interference contact with the rotor at rest. A small gap between the rotor and the top foil, i.e. bearing clearance, is created as the rotor speed increases while pushing away the top foil.
[3] The top foil and bump strip layer around the shim locations make a smooth contour for a radial assembly clearance.

Figures 11a – 11c illustrate the predicted mid-plane pressure, top foil deflection, and film thickness versus angular location for the original and shimmed GFBs operating at increasing rotor speeds. Note that the top foil extends from 45 º to 395 º. For a small static load of 6.5 N, i.e. a fraction of the rotor mass for the drive end bearing, the GFB with shims generates significant hydrodynamic pressures with peaks at three shim locations, while the original GFB shows much lower hydrodynamic pressures, irrespective of the rotor speeds. As the rotor speed increases, the hydrodynamic pressures, structural deflections and minimum film thickness also increase for the GFB with shims. In Fig. 11b, the model prediction shows a sagging effect in the top foil deflection and also produces "negative" values for at locations in between two shims. Note that although the GFB with shims enhances the hydrodynamic pressure generation thus implying an increase in bearing stiffness, a reduction in the minimum film thickness, in particular at low rotor speeds, may lead to earlier rotor touch-down, which is undesirable from the viewpoint of top foil and shat coatings endurance.

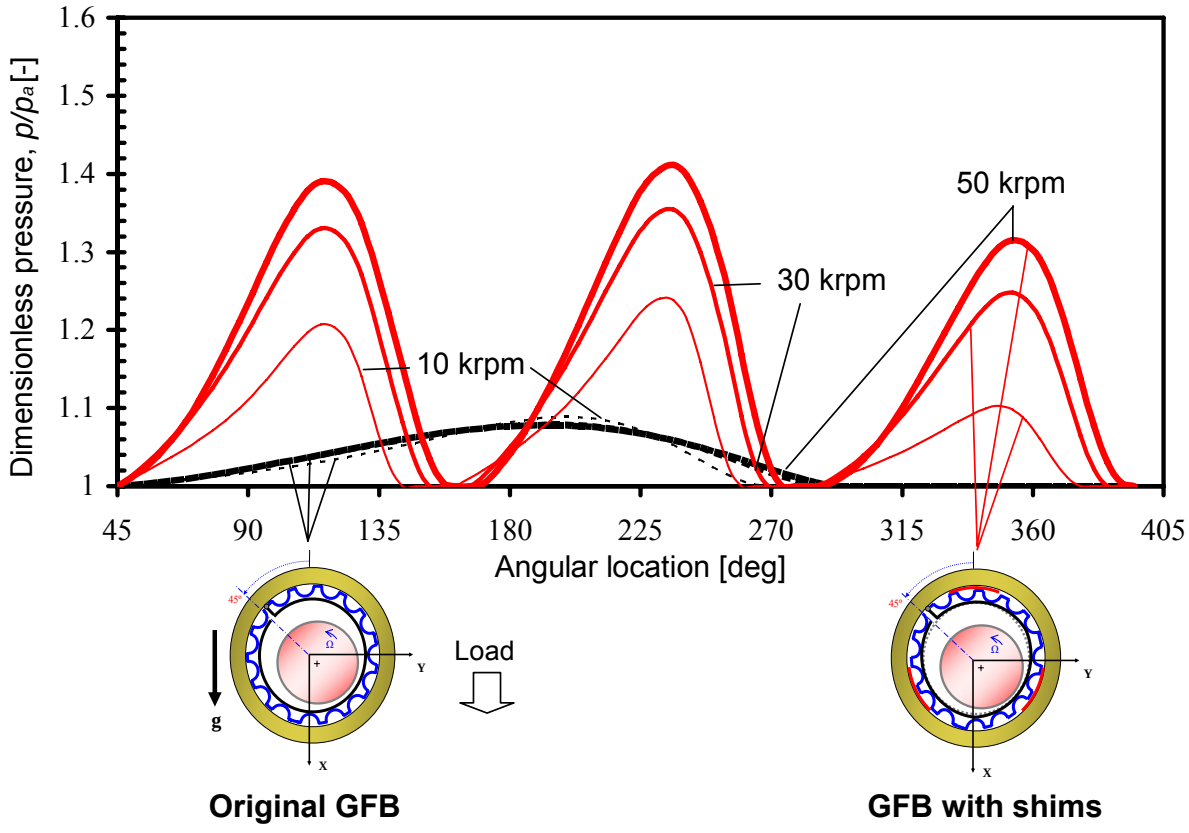

Figure 11a. Dimensionless mid-plane pressure versus angular location for original and shimmed GFBs at increasing rotor speeds. Static load of 6.5 N.

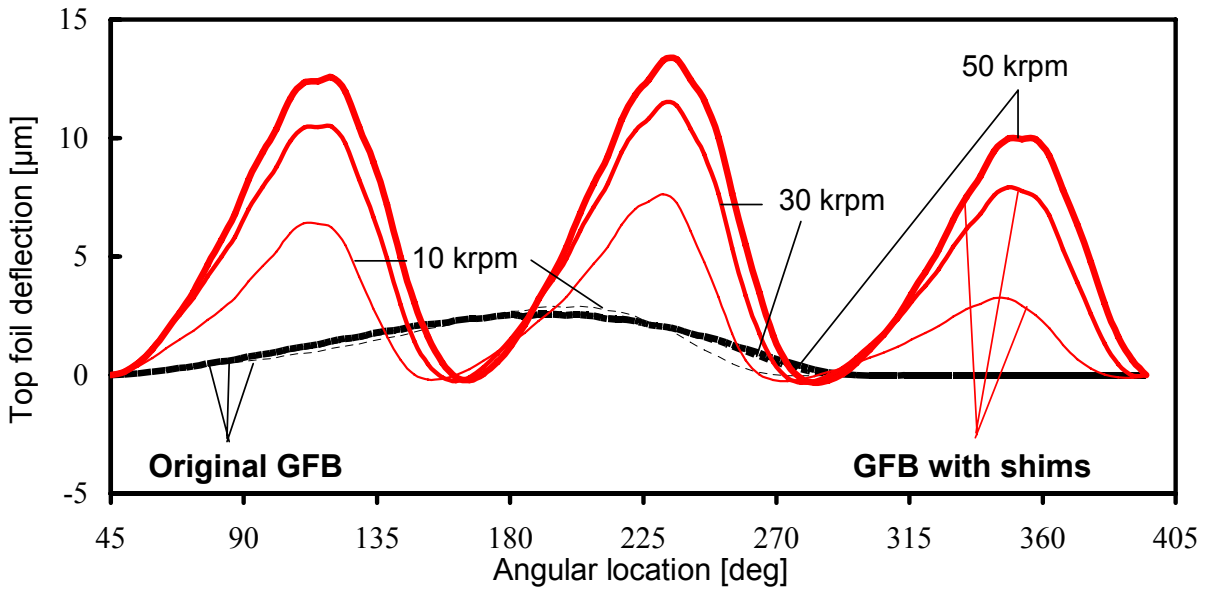

Figure 11b. Mid-plane top foil deflection versus angular location for original and shimmed GFBs at increasing rotor speeds. Static load of 6.5 N.

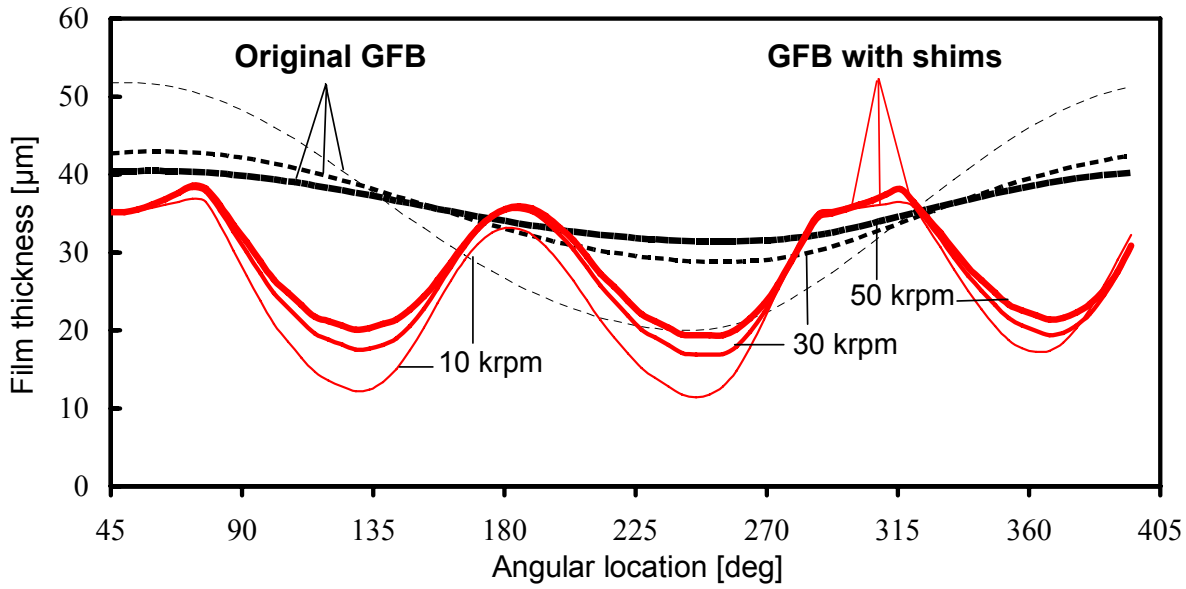

Figure 11c. Mid-plane film thickness versus angular location for original and shimmed GFBs at increasing rotor speeds. Static load of 6.5 N.

Figures 12 and 13 display the predicted journal eccentricity versus rotor speed and journal attitude angle versus rotor speed, respectively, for the original GFB and shimmed GFB. A nominal radial clearance of 35 μm is used for both GFBs. The shimmed GFB has smaller journal eccentricity and attitude angle when compared to the original GFB. Note that the smaller journal attitude angle for the shimmed GFB implies lesser cross-coupled effects. See Appendix A for journal eccentricity versus rotor speed and journal attitude angle versus rotor speed for the (original and shimmed) free end GFBs. Recall Fig. 2 for the configuration of test rotor and the designation of the two GFBs.

Figures 14 and 15 present the predicted synchronous force (stiffness and damping) coefficients versus rotor speed for the original and shimmed GFBs, respectively. A structural loss factor γ = 0.2 for the original and the shimmed GFBs represents energy dissipation from dry-friction effects [36]. Installation of shims into the GFBs leads to an increase in direct stiffness (K_{XX}, K_{YY}) and direct damping (C_{YY}) coefficients. Changes in other coefficients are relatively small. Stiffness ($K_{XX} \sim K_{YY}$ and $K_{XY} \sim -K_{YX}$) damping ($C_{XX} \sim C_{YY}$ and $-C_{XY} \sim C_{YX}$) coefficients for the shimmed GFBs indicate an almost centered rotor operation over the entire rotor speed range. For both the original and shimmed GFBs, the magnitudes of direct stiffness (K_{XX}, K_{YY}) are larger than those of cross-coupled stiffness (K_{XY}, K_{YX}), in particular at high rotor speeds, thus favoring stable rotor performance. Appendix B provides the predicted stiffness and damping coefficients for the original and shimmed free end GFBs.

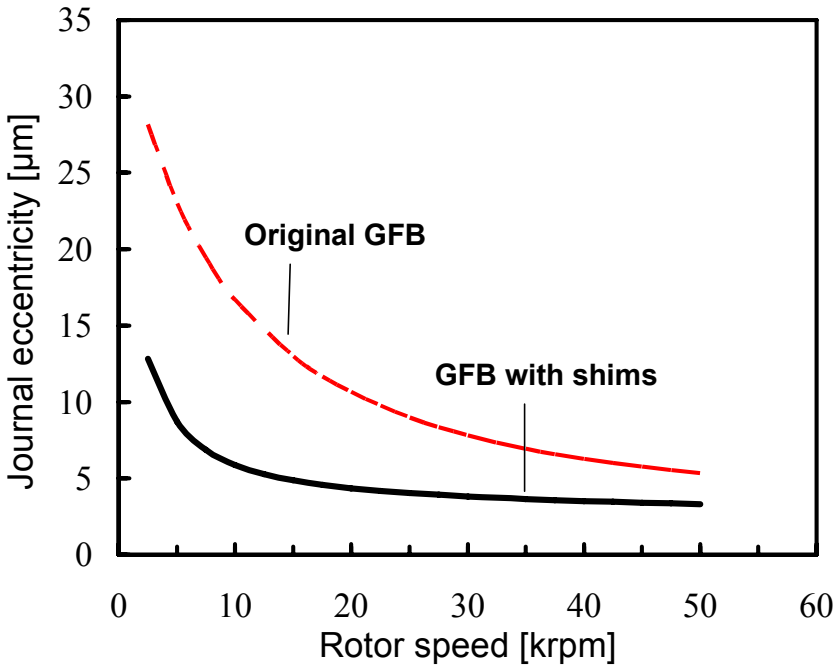

Figure 12. Predicted journal eccentricity versus rotor speed for original and shimmed GFBs. Static load of 6.6 N in vertical (*X*) direction. Drive end bearing.

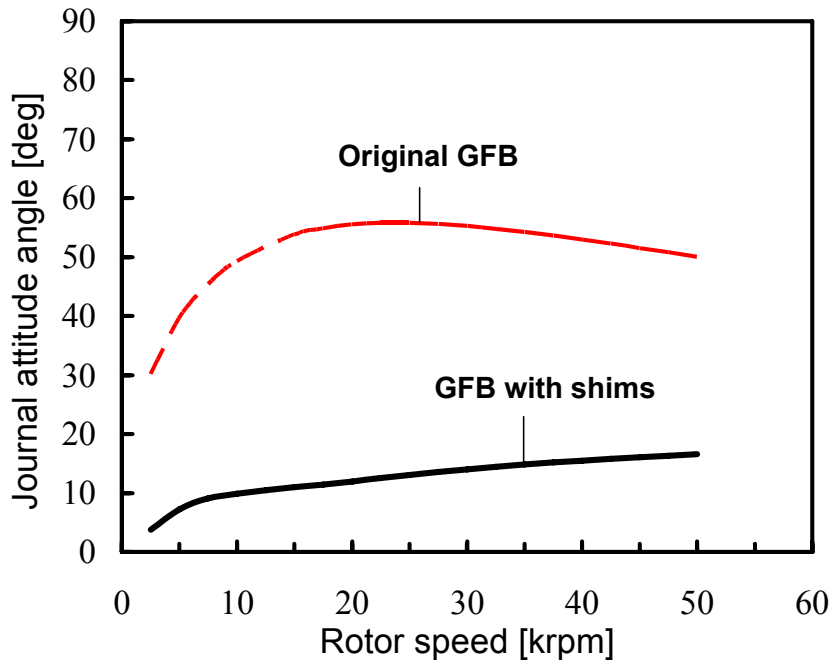

Figure 13. Predicted journal attitude angle versus rotor speed for original and shimmed GFBs. Static load of 6.6 N in vertical (*X*) direction. Drive end bearing.

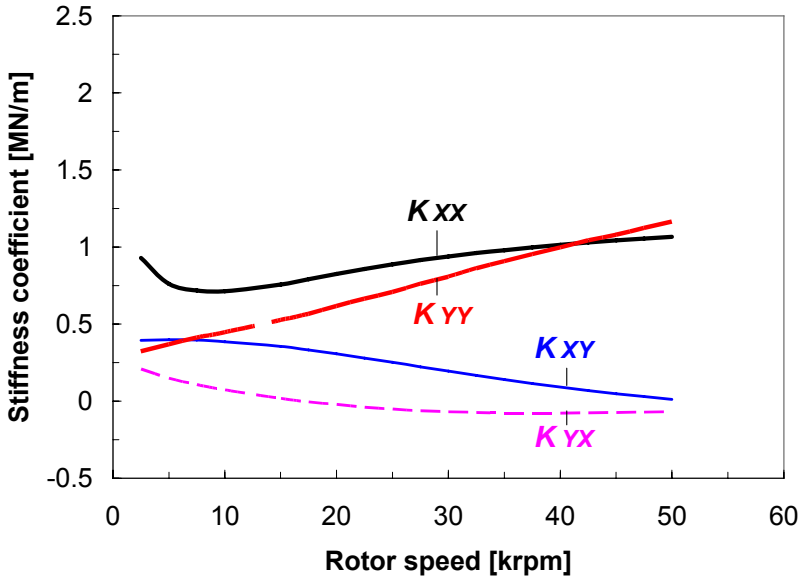

(a) Stiffness coefficients

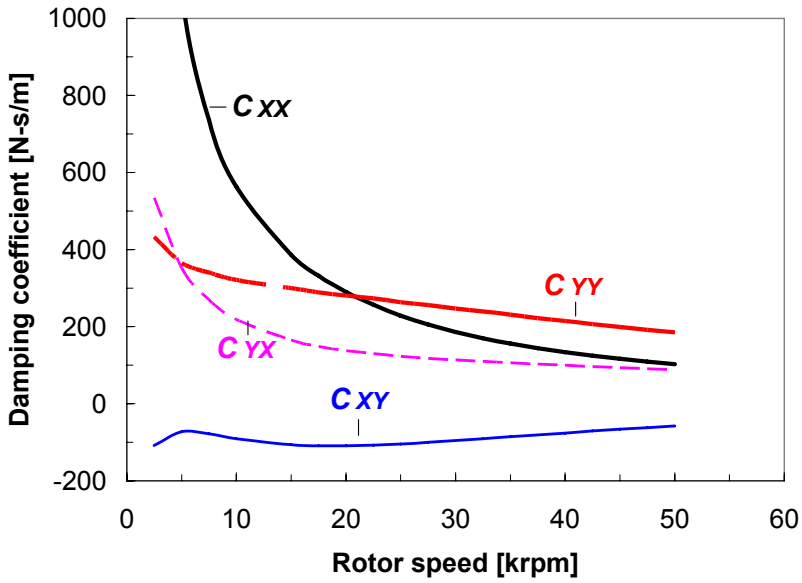

(b) Damping coefficients

Figure 14. Synchronous stiffness and damping coefficients versus rotor speed for original GFBs. Static load of 6.6 N in vertical (*X*) direction. Structural loss factor, *γ* = 0.2. Drive end bearing.

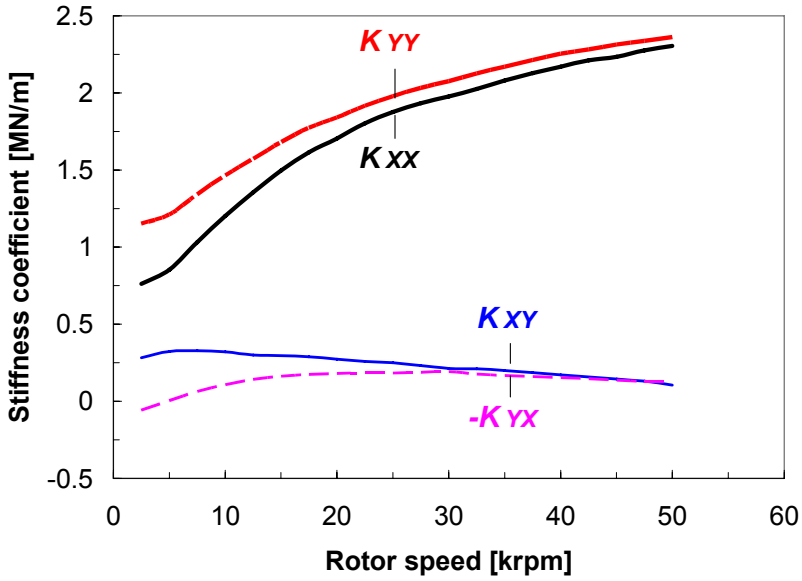

(a) Stiffness coefficients

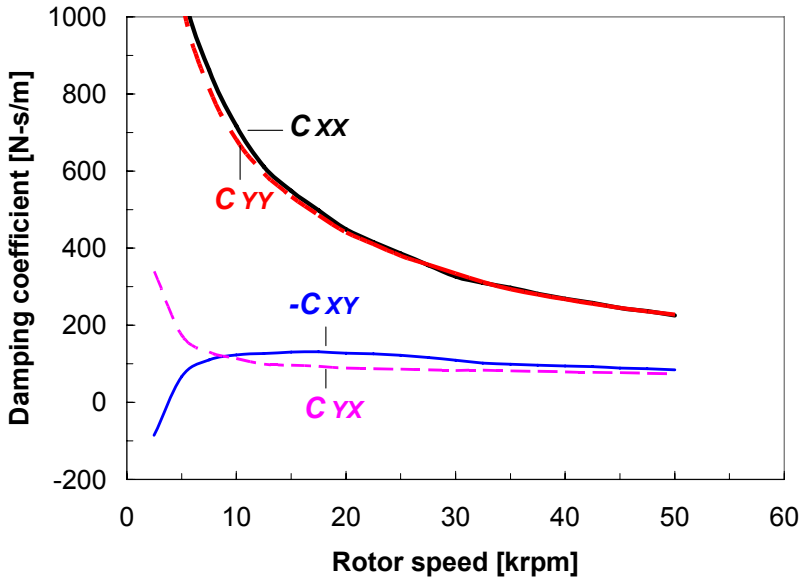

(b) Damping coefficients

Figure 15. Synchronous stiffness and damping coefficients versus rotor speed for GFBs with shims. Static load of 6.6 N in vertical (*X*) direction. Structural loss factor, *γ* = 0.2. Drive end bearing.

V. ROTOR RESPONSE PREDICTIONS COMPARED TO TEST DATA.

V-1. FINITE ELEMENT MODEL FOR ROTOR - BEARING SYSTEM

In the companion report [5], test measurements of rotor synchronous responses verify the linearity of the test rotor – GFBs system. A linear rotordynamics software (XLTRC^2®) models the test rotor – GFBs system and predicts the rotor synchronous responses. Figure 16 shows the finite element structural model of the test rotor. The flexible coupling used in Ref. [23] is replaced with a softer one, i.e., the old and new coupling have estimated lateral stiffness coefficients of 1.63×10^5 N/m and 1×10^3 N/m, respectively. The connecting shaft in Ref. [23] is also replaced with a longer one of the same material, i.e., old and new connecting shafts have lengths of 30 mm and 46 mm, respectively. The modifications aid to isolate the rotor - GFB system from the drive motor system. See Refs. [5,35] for a detailed description of the test rig.

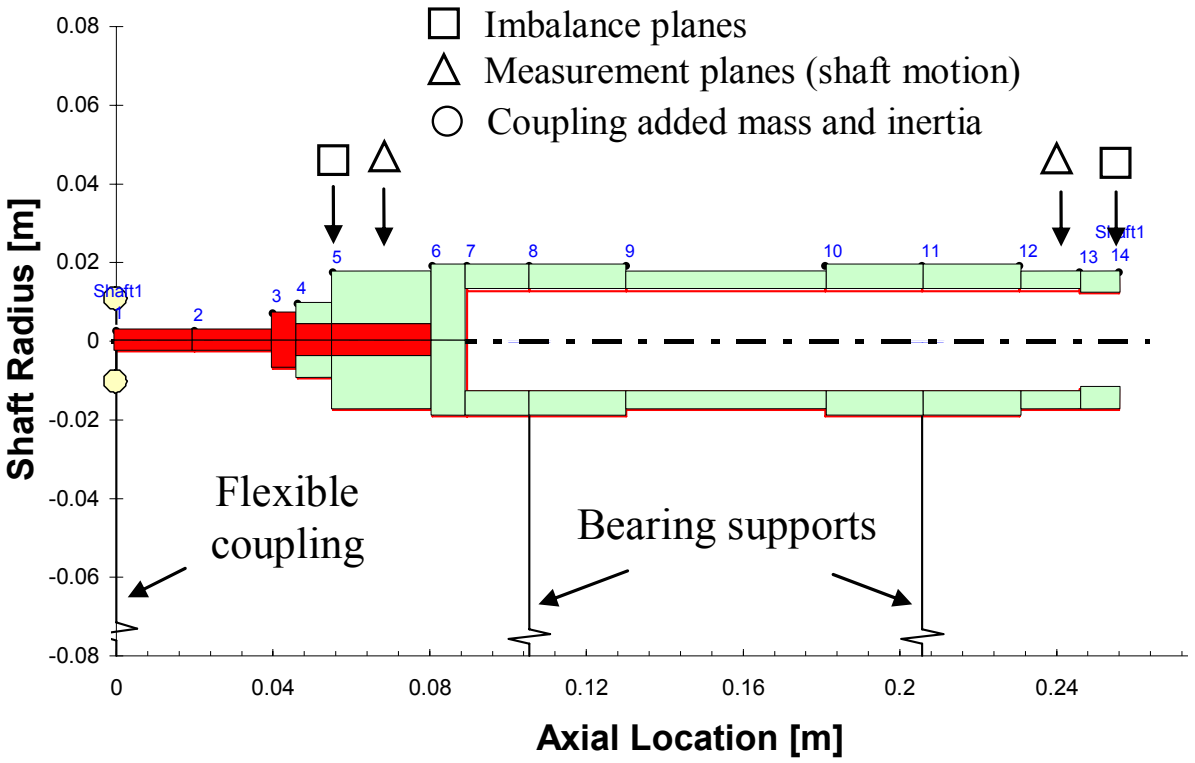

Figure 16. Finite element model of test rotor supported on two radial GFBs (with connecting shaft and flexible coupling)

V-2. ORIGINAL FOIL GAS BEARINGS

An eigenvalue analysis predicts the rotor-GFBs system damped natural frequencies and damping ratios for the test speed range, using the predicted stiffness and damping coefficients[4] for original GFBs as shown in Figs. 14 and B1. No side feed pressure is assumed for the model predictions compared to test measurements at a low side pressure of 0.35 bar (5 psig).

Figure 17 shows the damped natural frequency map and predicted forward mode critical speeds at 3.25 krpm and 4.0 krpm, associated to cylindrical and conical modes, respectively. Figure 18 shows predicted damping ratios decreasing rapidly as rotor speed increases. A positive damping ratio indicates a stable system. Predicted damping ratios of ~ 0.5 at the critical speeds denote a well damped system.

Figures 19a and 19b compare the predicted phase angle and normalized rotor amplitude of synchronous responses to test measurements recorded during rotor speed coastdown tests from 25 krpm [5] for in-phase and out-of-phase imbalance masses of 55 mg, 110 mg, 165 mg, and 330 mg at the drive end bearing location. The imbalance masses are added into the rotor end planes at radius (r) equal to 15.11 mm. For the smallest mass of 55 mg, imbalance displacements (u) are 1.3 μm and 2.3 μm (bases for normalization) at the drive and free end bearings, respectively [5]. Note that the prediction based on linearized bearing force coefficients shows a unique curve. In general, the predictions are in good agreement with test data, phase angle and amplitude, for small to moderate imbalance masses, i.e. 55 mg to 165 mg, i.e. characteristic of a linear system. The rotor critical speed, where the rotor amplitude is largest, is determined at rotor speed higher than a system natural frequency, i.e. $\omega_{cr} = \omega_n / \sqrt{1-2\varsigma^2}$ [37].

On the other hand, for the largest imbalance mass of 330 mg, the comparison evidences a large discrepancy, in particular for rotor amplitudes around the system critical speed and phase angle above that speed. An increase in normalized rotor amplitude and different trend in phase angle from those obtained for small to moderate imbalance masses are attributed to the system nonlinearity due to a reduction in viscous damping [5]. Note that, without viscous damping, the rotor critical speed approaches the system natural frequency, i.e. $\omega_{cr} \rightarrow \omega_n$. See Ref. [5] for a more detailed description. Appendix C provides a comparison of the predicted synchronous responses to test measurements at the free end bearing. All predicted and measured synchronous

[4] Predicted stiffness and damping coefficients for a nominal radial clearance of 35 μm, shown in Figs. 12, 13, B1, and B2 are used for original and shimmed GFBs.

rotor amplitudes approach the imbalance displacements (u) of 1.3 μm and 2.3 μm at the drive and free end bearing locations, respectively, as the rotor speed increases.

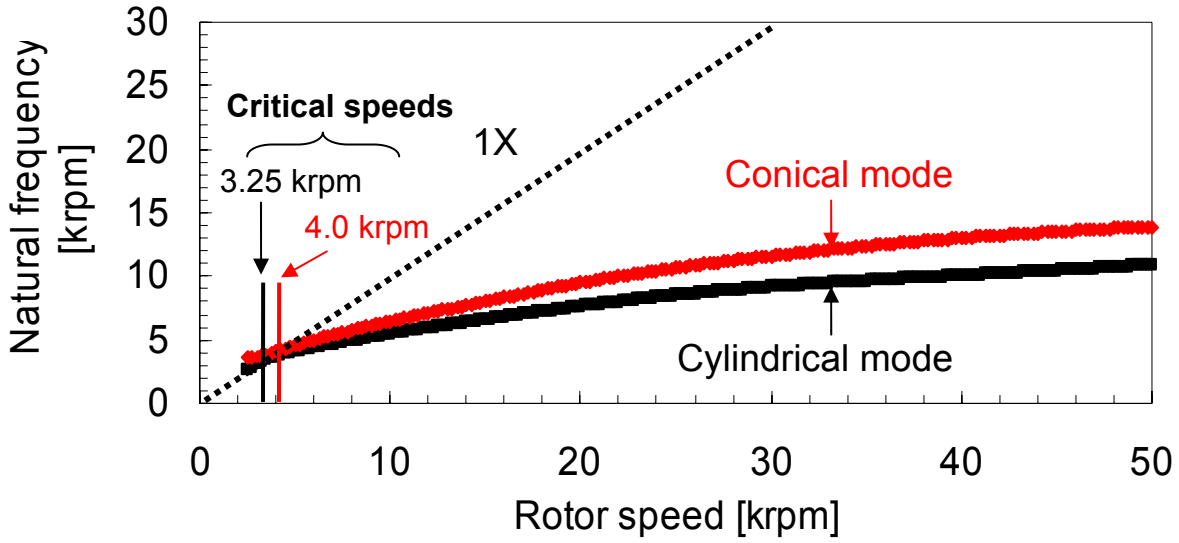

Figure 17. Predicted damped natural frequencies for rotor – GFB system (forward modes). Original GFBs.

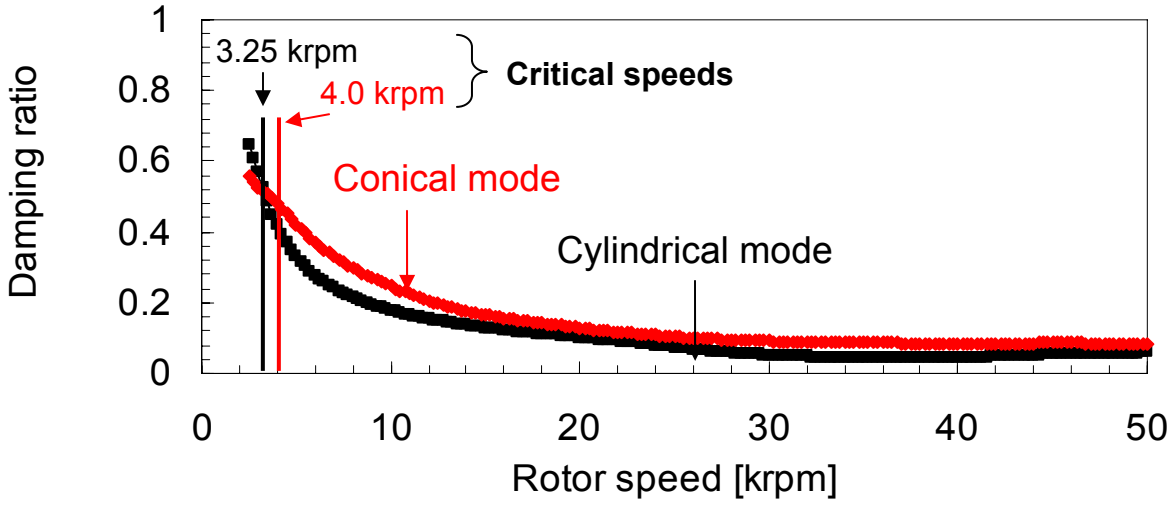

Figure 18. Predicted damping ratios (ς) for rotor – GFB system. Original GFBs.

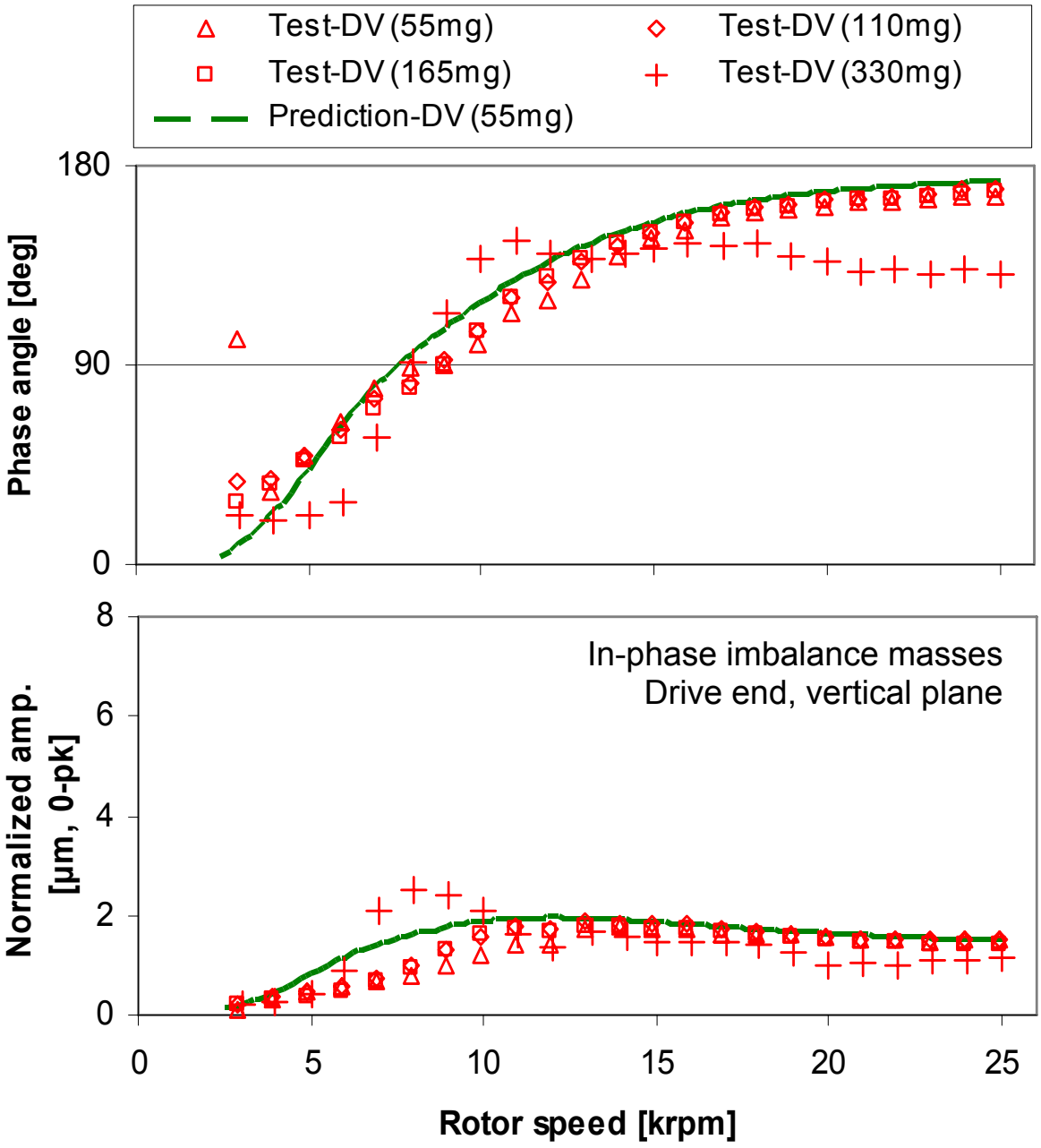

Figure 19a. Phase angle and normalized rotor amplitude of synchronous response for increasing in-phase imbalance mass. Drive end, vertical plane. Predictions compared to test data. Original GFBs.

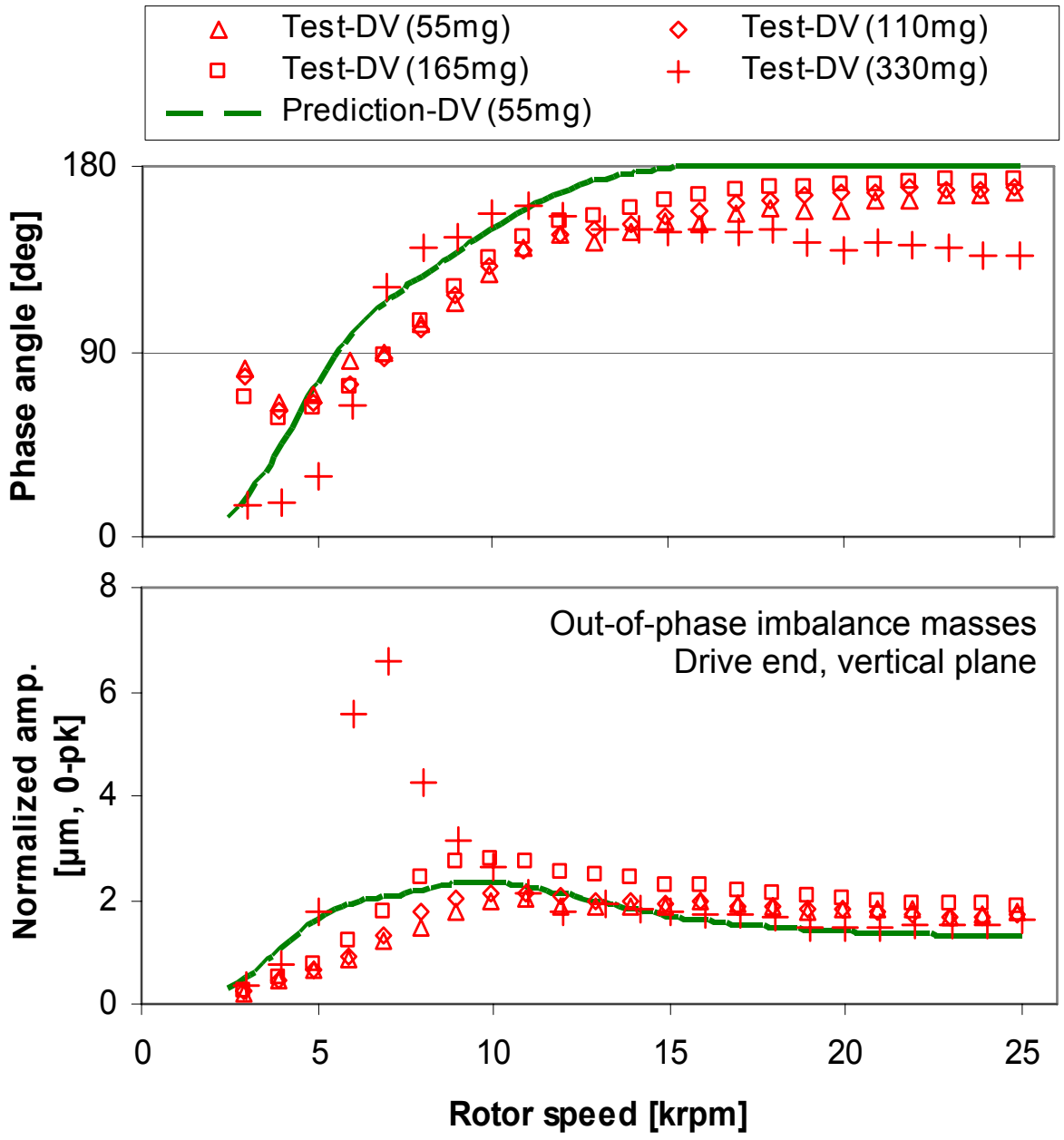

Figure 19b. Phase angle and normalized rotor amplitude of synchronous response for increasing Out-of-phase imbalance mass. Drive end, vertical plane. Predictions compared to test data. Original GFBs.

V-3. SHIMMED FOIL GAS BEARINGS

Figures 20 and 21 present the damped natural frequency map with forward mode critical speeds and damping ratios, respectively, for the rotor- shimmed GFBs system. The predicted stiffness and damping coefficients in Figs. 15 and B2 are used in the rotordynamic prediction; but the damping coefficients are arbitrarily doubled[5]. The critical speeds at 7.5 krpm and 11 krpm are associated to conical and cylindrical modes, respectively. The positive damping in the speed range indicates rotordynamically stable rotor operation to 50 krpm.

Figures 22a and 22b compare the predicted phase angle and normalized rotor amplitude of synchronous responses to test measurements recorded during rotor coastdown tests from 35 krpm [5] for in-phase and out-of-phase imbalance masses of 55 mg and 110 mg at the drive end bearing locations. In general, the predictions agree reasonably with test data, phase angle and amplitude, for small to moderate imbalance masses, i.e. 55 mg to 110 mg. See Appendix C for a comparison of the predicted synchronous responses to test measurements at the free end bearing.

[5] The structural loss factor for the shimmed GFBs is unknown. However, installation of shims is expected to facilitate dry-friction of the bumps, in particular at low rotor speeds, thus dissipating more energy. Presently, damping coefficients for the shimmed GFBs, predicted using a structural loss factor of 0.2, are arbitrarily doubled, i.e. $2\times C$'s for the rotordynamic analysis. Note that, for the light weight test rotor, an increase in the structural loss factor does not increase significantly the bearing damping coefficients, in particular at low rotor speeds.

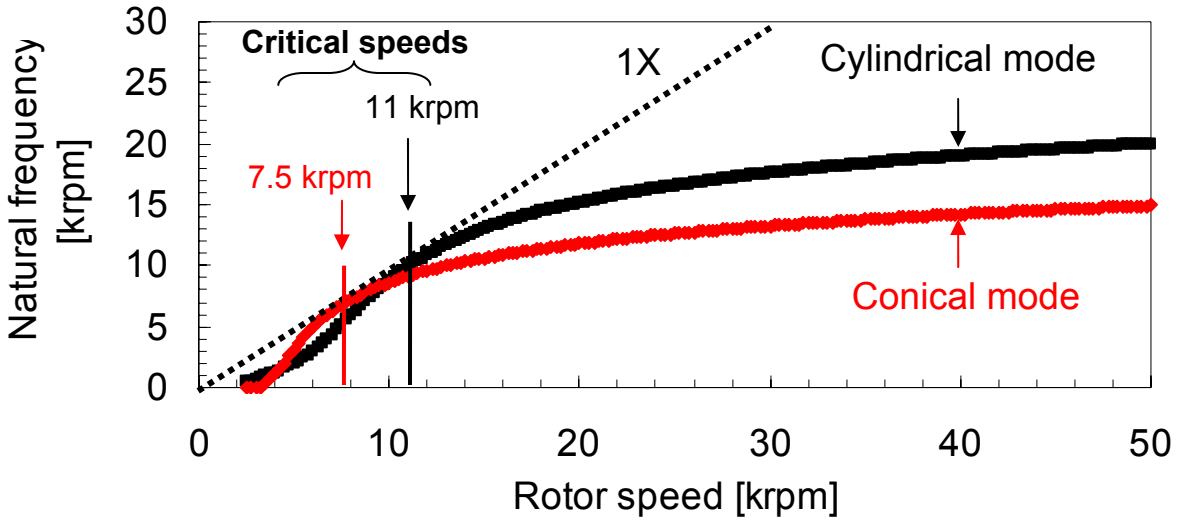

Figure 20. Predicted damped natural frequencies for rotor – GFB system (forward modes). GFBs with shims.

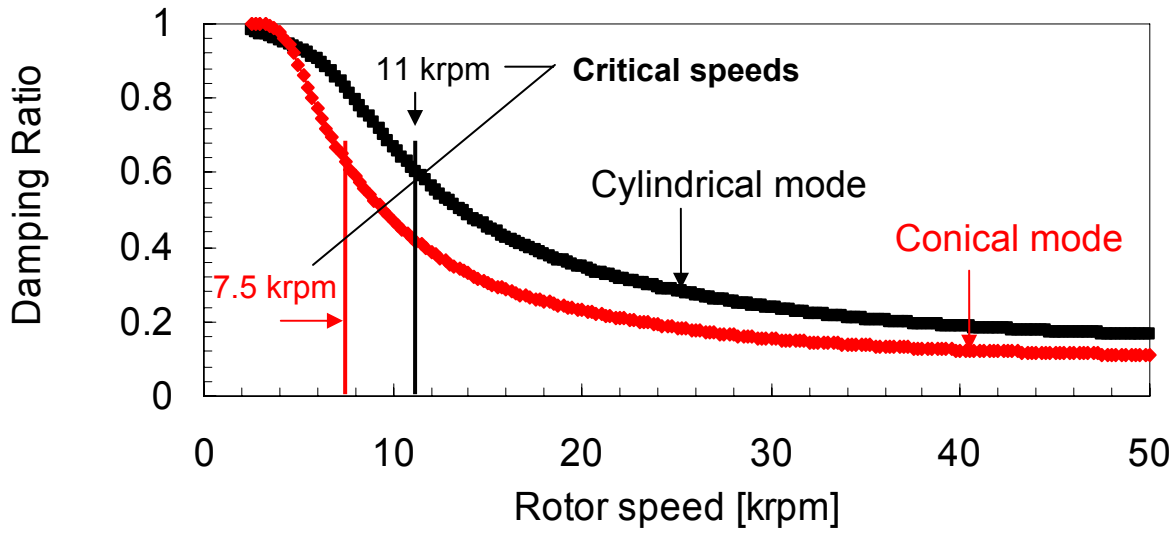

Figure 21. Predicted damping ratios for rotor – GFB system. GFBs with shims.

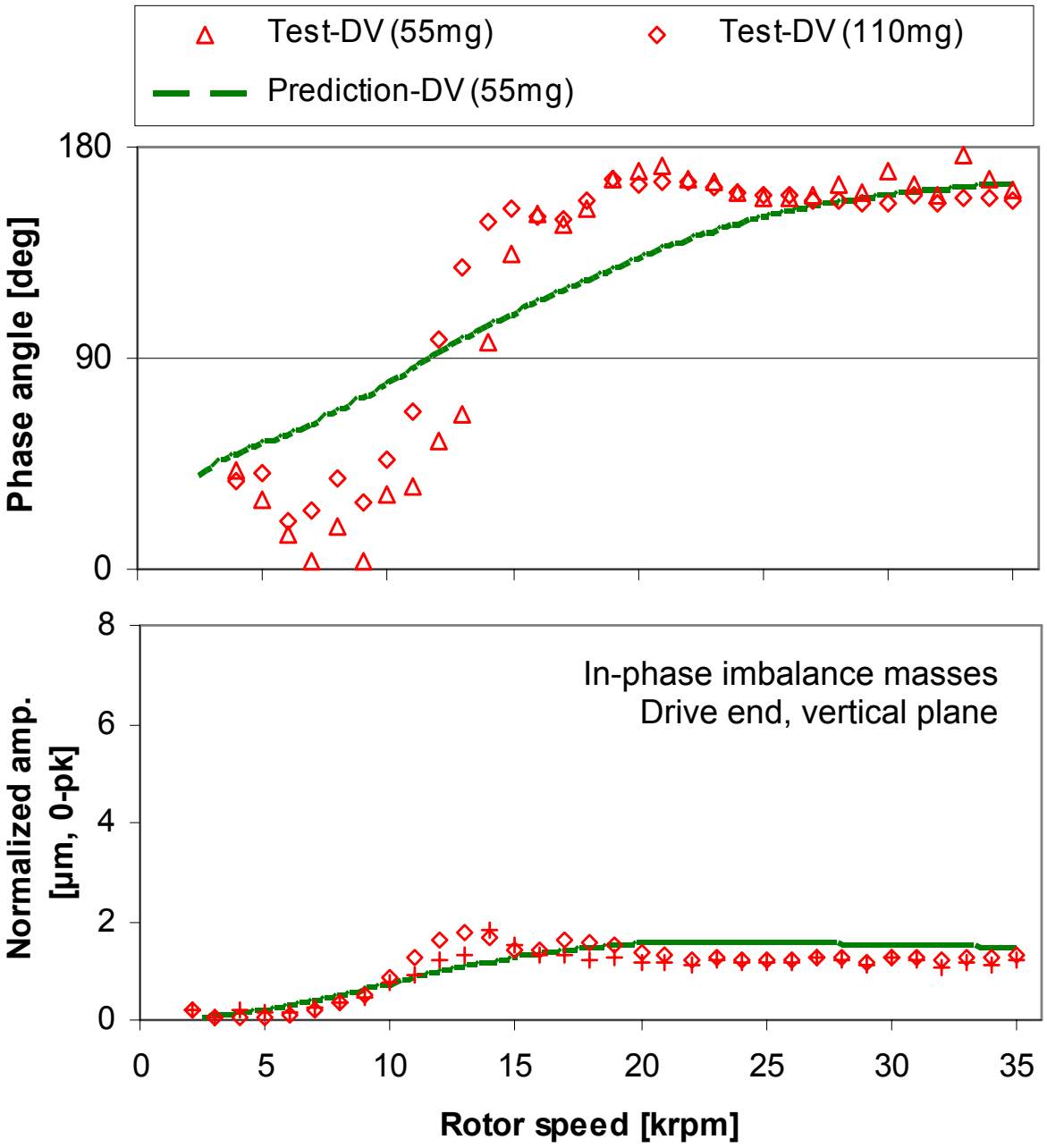

Figure 22a. Phase angle and normalized rotor amplitude of synchronous response for increasing in-phase imbalance mass. Drive end, vertical plane. Predictions compared to test data.

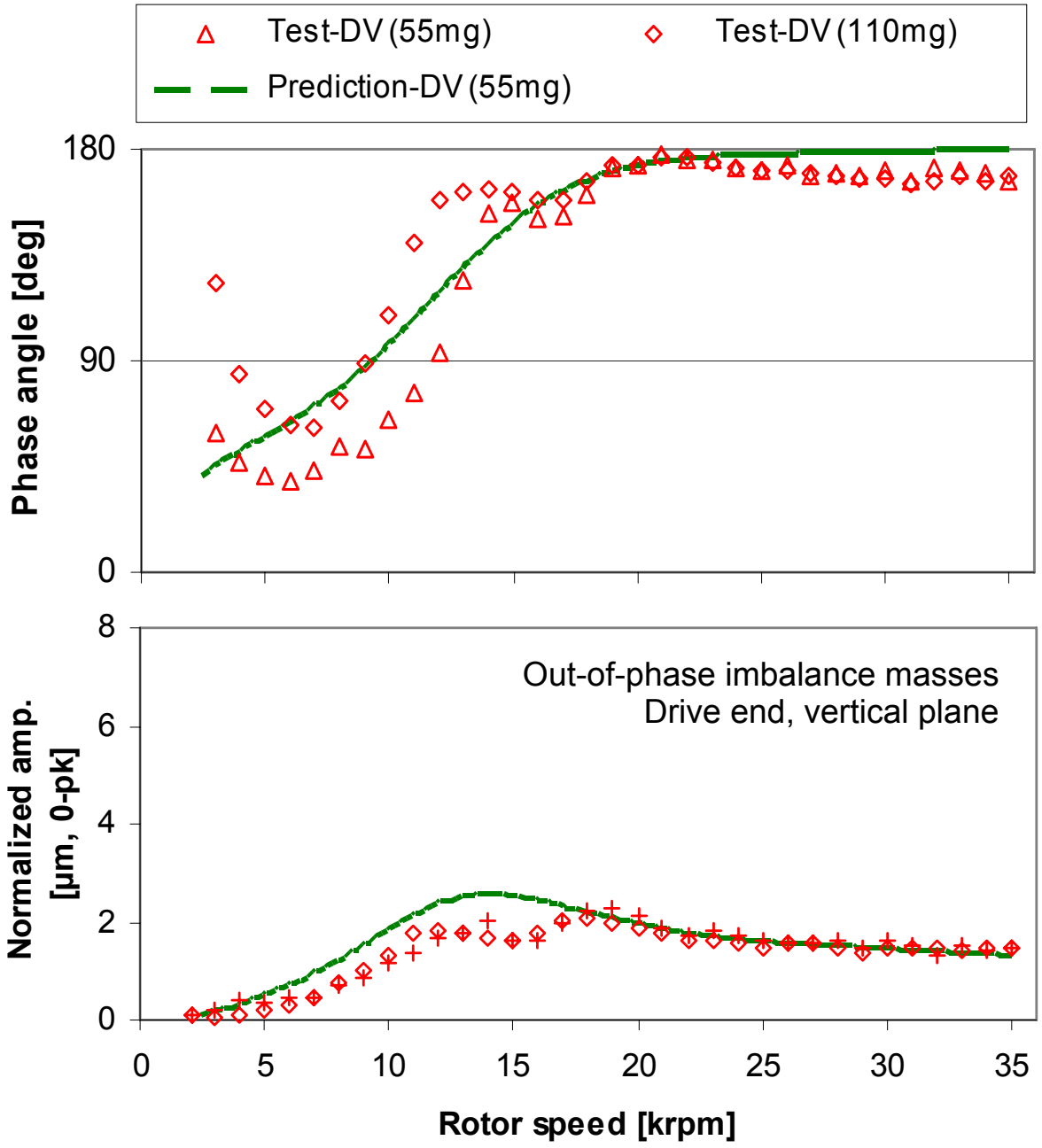

Figure 22b. Phase angle and normalized rotor amplitude of synchronous response for increasing out-of-phase imbalance mass. Drive end, vertical plane. Predictions compared to test data.

VI. CONCLUSIONS

The report presents an analysis of gas foil bearings (GFBs) with side feed pressurization. Model predictions show that the bearing direct stiffness and damping coefficients increase, but the difference in cross-coupled stiffnesses, K_{XY}-K_{YX}, decreases as the side pressure increases. The analysis shows that a sufficiently high side feed pressure effectively retards the evolution of the circumferential gas velocity, thus ensuring a stable rotor operation. The prediction shows good agreement with test data.

A model for GFBs with a machined mechanical preload introduced in 2006 TRC report is upgraded to predict the performance of shimmed GFBs. A sinusoidal function approximately depicts the assembly radial clearance modified due to installation of three shims. A GFB with shims generates significant hydrodynamic pressures with peaks at the three shim locations, while the original GFB shows much lower pressures, irrespective of rotor speed. Note that although the GFB with shims enhances the bearing direct stiffness, a reduction in the minimum film thickness, in particular at low rotor speeds, may lead to earlier rotor touch-down, which is undesirable for top foil and shaft coating endurance.

A finite element (FE) model of the test rotor-GFB system is developed using XLTRC^2©). A soft flexible coupling and connecting shaft aid to isolate the rotor –GFB system from the drive motor system. An eigenvalue analysis predicts the system critical speeds and damping ratios for the original and shimmed GFBs. In general, predicted rotor synchronous responses based on linearized bearing coefficients show good agreement with test measurements. Discrepancies between test data and predictions may be associated to uncertainties in the actual imbalance distribution.

Further extensive analyses anchored to test data are required to improve the accuracy in performance prediction of GFBs operating in high temperature environments. A lumped parameter thermal model for transport of energy within a GFB will account for heat flux through the gas film and into the bearing structure.

VII. REFERENCES

[1] Agrawal, G. L., 1997, "Foil Air/Gas Bearing Technology – an Overview," ASME Paper No. 97-GT-347.

[2] Salehi, M., Heshmat, H., Walton, J. F., and Tomaszewski, M., 2007, "Operation of a Mesoscopic Gas Turbine Simulator at Speeds in Excess of 700,000 rpm on Foil Bearings," ASME J. Eng. Gas Turbines Power, **129**, pp. 170-176.

[3] http://www.eere.energy.gov/afdc/apps/toolkit/pdfs/mod08_zebs.pdf, accessed May 04, 2007.

[4] Bauman, S., 2005, "An Oil-Free Thrust Foil Bearing Facility Design Calibration, and Operation," NASA/TM-2005-213568.

[5] Kim, T. H., and San Andrés, L., 2007, "Effect of Side Feed Pressurization on the Performance of Shimmed Foil Gas Bearings – Part I: Experimental Verification," Technical Report No TRC-B&C-2-07, Texas A&M Univ., College Station, TX.

[6] San Andrés, L., and T-H Kim, 2007, "Improvements to the Analysis of Gas Foil Bearings: Integration of Top Foil 1D and 2D Structural Models," ASME Paper No. GT2007-27249.

[7] Lund, J. W., 1968, "Calculation of Stiffness and Damping Properties of Gas Bearings," ASME J. Lubr. Technol., **90**, pp 793-803.

[8] San Andrés, L., and Kim, T. H., 2006, "Computational Analysis of Gas Foil Bearings Integrating 1D and 2D Finite Element Models for Top Foil," Technical Report No TRC-B&C-1-06, Texas A&M Univ., College Station, TX.

[9] Heshmat, H., Walowit, J. A., and Pinkus, O., 1983, "Analysis of Gas-Lubricated Foil Journal Bearings," ASME J. Lubr. Tech., **105**, pp. 647-655.

[10] Heshmat, H., Walowit, J. A., and Pinkus, O., 1983, "Analysis of Gas Lubricated Compliant Thrust Bearings," ASME J. Lubr. Tech., **105**, pp. 638-646.

[11] Carpino M., Talmage, G., 2003, "A Fully Coupled Finite Element Formulation for Elastically Supported Foil Journal Bearings," STLE Tribol. Trans., **46**, pp. 560-565.

[12] Carpino M., Talmage, G., 2006, "Prediction of Rotor Dynamic Coefficients in Gas Lubricated Foil Journal Bearings with Corrugated Sub-Foils," STLE Tribol. Trans., **49**, pp. 400-409.

[13] Lee, Y.-B., Park, D.–J., and Kim, C.–H., 2006, "Numerical Analysis for Bump Foil Journal Bearing Considering Top Foil Effect and Experimental Investigation," Paper-ID 229, *Proc. 7th IFToMM-Conference on Rotor Dynamics*, Vienna, Austria.

[14] Peng, J.-P., and Carpino, M., 1994, "Coulomb Friction Damping Effects in Elastically Supported Gas Foil Bearings," STLE Tribol. Trans., **37**(1), pp. 91-98.

[15] Ruscitto, D., Mc Cormick, J., and Gray, S., 1978, "Hydrodynamic Air Lubricated Compliant Surface Bearing For An Automotive Gas Turbine Engine I-Journal Bearing Performance," NASA CR-135368.

[16] Kim, T. H., and San Andrés, L., 2005, "Heavily Loaded Gas Foil Bearings: a Model Anchored to Test Data," ASME Paper No. GT2005-68486.

[17] Heshmat, C. A., Xu, D. S., and Heshmat, H., 2000, "Analysis of Gas Lubricated Foil Thrust Bearings Using Coupled Finite Element and Finite Difference Methods," ASME J. Tribol., **122,** pp. 199-204.

[18] Heshmat, H., Chen, H. M., and Walton, J. F., 2000, "On the Performance of Hybrid Foil-Magnetic Bearings," ASME J. Eng. Gas Turbines Power, **122**, pp. 73-81.

[19] Peng, Z.-C., and Khonsari, M. M., 2004, "On the Limiting Load-Carrying Capacity of Foil Bearings," ASME J. Tribol., **126**, pp. 817-818.

[20] Radil, K., Howard, S., and Dykas, B., 2002, "The Role of Radial Clearance on the Performance of Foil Air Bearings," STLE Tribol. Trans., **45**, pp. 485-490.

[21] Kim, T.H., and L. San Andrés, 2006, "Limits for High Speed Operation of Gas Foil Bearings," ASME Journal of Tribology, 128, pp. 670-673.

[22] Mohawk Innovative Technology, Inc., 2004, "Foil Gas Bearings Enable Oil-Free Compressor Breakthrough," Newsletter Vol. 19, http://www.miti.cc/newsletters/19_ foil_gas _bearings_enable_oilfree_compressor_breakthrough.pdf, accessed May 04, 2007.

[23] San Andrés, L., D. Rubio, and T.H. Kim, 2006, "Rotordynamic Performance of a Rotor Supported on Bump Type Foil Gas Bearings: Experiments and Predictions," ASME Paper GT 2006-91238 (to appear in ASME Journal of Engineering for Gas Turbines and Power, Vol. 129, 2007).

[24] Allaire, P. E., Lee, C. C., and Gunter, E. J., 1978, "Dynamics of Short Eccentric Plain Seals with High Axial Reynolds Numbers," J Spacecraft and Rockets, **15**, pp. 341-347.

[25] Childs, D., 1993, *Turbomachinery Rotordynamics – Phenomena, Modeling, & Analysis*, John Wiley & Sons, New York, pp. 248–274.

[26] Black, H. F., Allaire, P. E., and Barrett, L. E., 1981, "Inlet Flow Swirl in Short Turbulent Annular Seal Dynamics," *Proc. the Ninth Intl. Conf. in Fluid Sealing*, BHRA Fluid Engineering, Leeuwenborst, The Netherlands.

[27] Dykas, B., and Howard, S. A., 2004, "Journal Design Consideration for Turbomachine Shaft Supported on Foil Air Bearings," STLE Tribol. Trans. **47**, pp. 508-516.

[28] Salehi, M., Swanson, E., and Heshmat, H., 2001, "Thermal Features of Compliant Foil Bearings – Theory and Experiments," ASME J. Tribol., **123**, pp. 566-571.

[29] Pinkus, O. and Bupara, S. S., 1979, "Adiabatic Solution for Finite Journal Bearings," ASME J. Lubr. Technol., **101**, pp. 492-496.

[30] Peng, Z-C., and Khonsari, M. M., 2006, "A Thermohydrodynamic Analysis of Foil Journal Bearings," ASME J. Tribol., **128**, pp. 534-540.

[31] Radil, K., and Zeszotek, M., 2004, "An Experimental Investigation into the Temperature Profiles of a Compliant Foil Air Bearing," STLE Tribol. Trans., **47**, pp.470-479.

[32] Heshmat, H., 1994, "Advancements in the Performance of Aerodynamic Foil Journal Bearings: High Speed and Load Capacity," ASME J. Tribol., **116**, pp. 287-295.

[33] Chen, H. M., Howarth, R. Geren, B., Theilacker, J. C., and Soyars, W. M., 2000, "Application of Foil Bearings to Helium Turbocompressor," *Proc.30^{tb} Turbomachinery Symposium*, Texas A&M Univ., Houston, TX, pp. 103-113.

[34] Kim, T. H., 2006, "Analysis of Gas Foil Bearings Integrating 1D and 2D Finite Element Structural Models - Predictions Compared to Test Data," Paper IMECE2006-16375, *ASME International Mechanical Engineering Congress and Exposition*, Chicago, IL, November.

[35] San Andrés, L., and Kim, T.H, 2006, "Further Imbalance Response Measurements of Rotor Supported on Bump-Type Gas Foil Bearings: Operation to 50 krpm," Technical Report No TRC-B&C-1-06, Texas A&M Univ., College Station, TX.

[36] Rubio, D., and L. San Andrés, 2007, "Structural Stiffness, Dry-Friction Coefficient and Equivalent Viscous Damping in a Bump-Type Foil Gas Bearing," ASME J. Eng. Gas Turbines Power, **129**(2), pp. 494-502.

[37] Ginsberg, J. H., 2001, *Mechanical and Structural Vibration – Theory and Application*, John Wiley & Sons, New York, pp. 135–139.

APPENDIX A. PREDICTED JOURNAL ECCENTRICITY AND ATTITUDE ANGLE VERSUS ROTOR SPEED FOR ORIGINAL AND SHIMMED GFBS. FREE END BEARING.

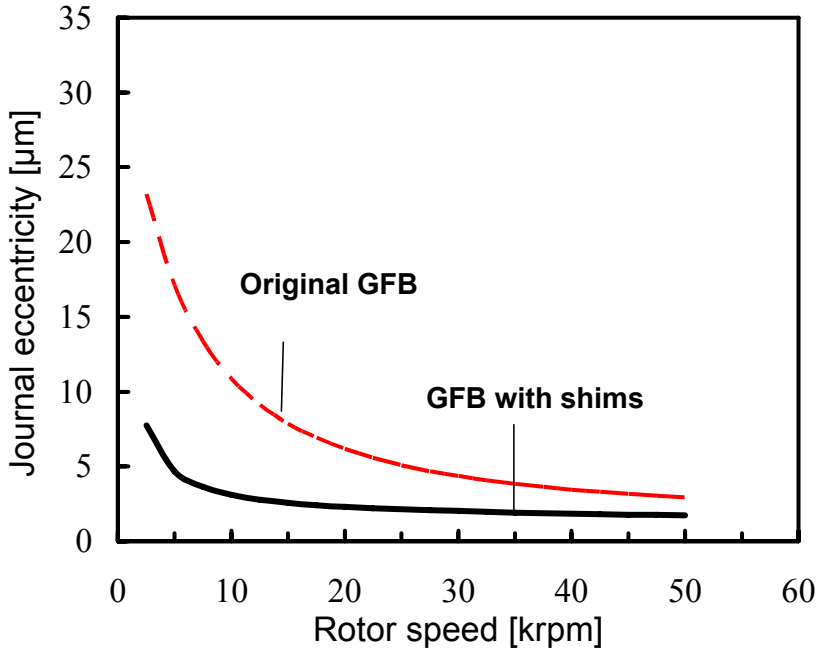

Figure A1. Predicted journal eccentricity versus rotor speed for original and shimmed GFBs. Static load of 6.6 N in vertical (*X*) direction. Free end bearing.

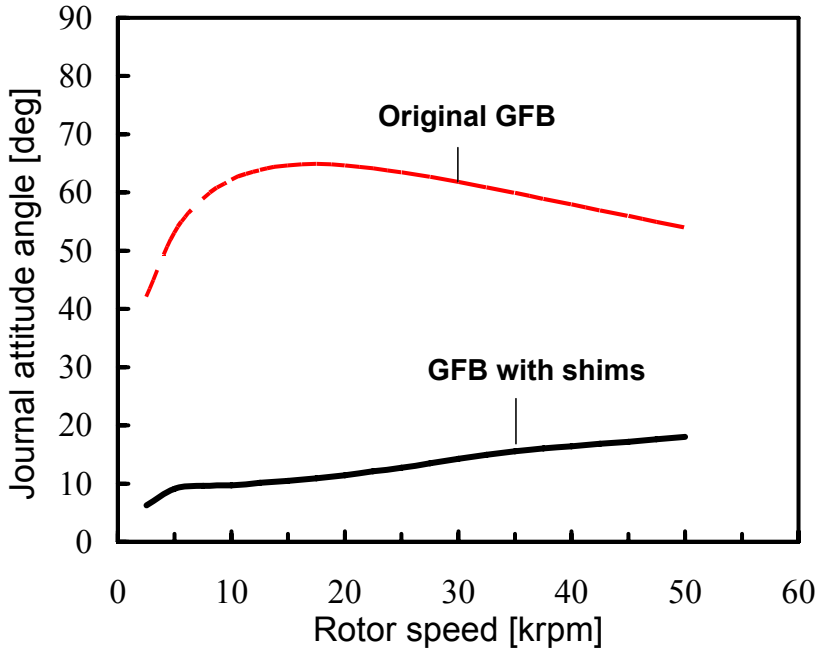

Figure A2. Predicted journal attitude angle versus rotor speed for original and shimmed GFBs. Static load of 6.6 N in vertical (*X*) direction. Free end bearing.

APPENDIX B. PREDICTED STIFFNESS AND DAMPING COEFFICIENTS VERSUS ROTOR SPEED. FREE END BEARING.

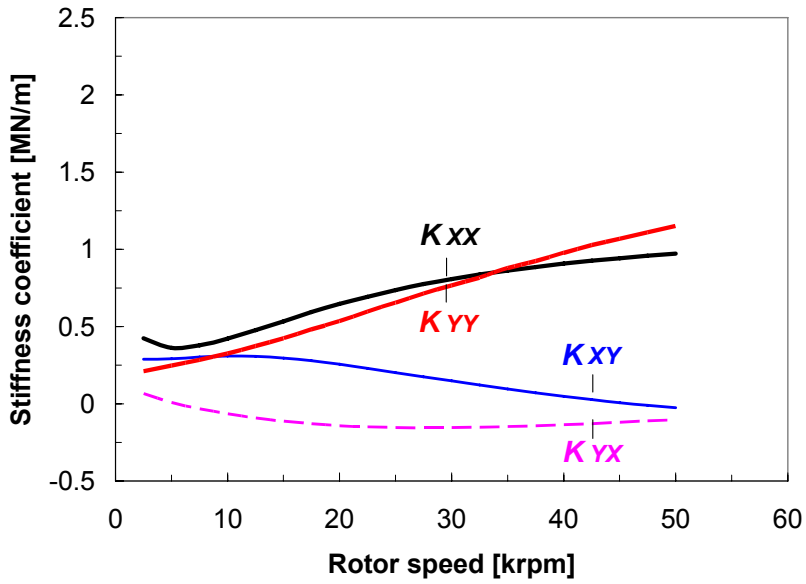

(a) Stiffness coefficients

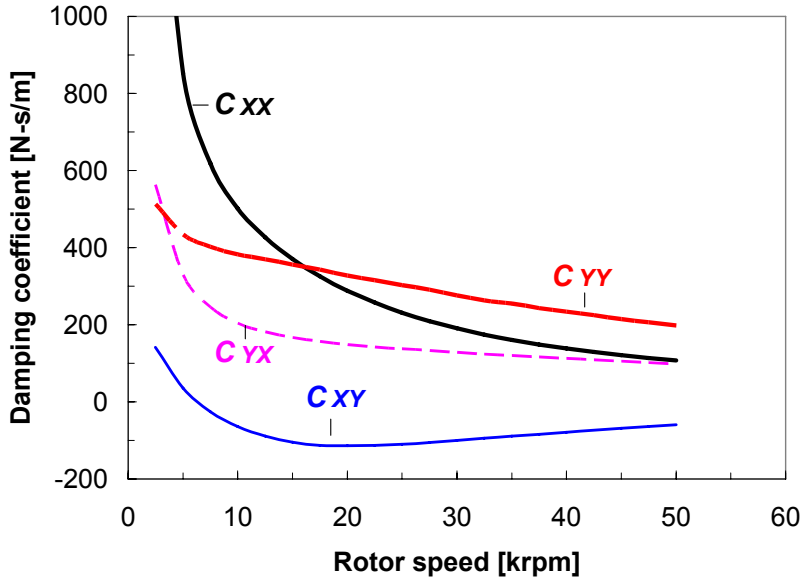

(b) Damping coefficients

Figure B1. Synchronous stiffness and damping coefficients versus rotor speed for Original GFBs. Static load of 3.6 N in vertical (*X*) direction. Structural loss factor, γ = 0.2. Free end bearing.

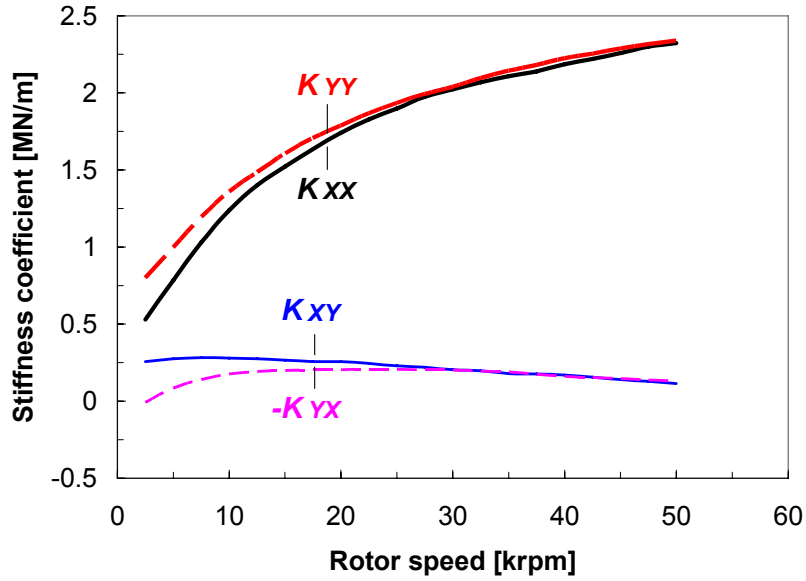

(a) Stiffness coefficients

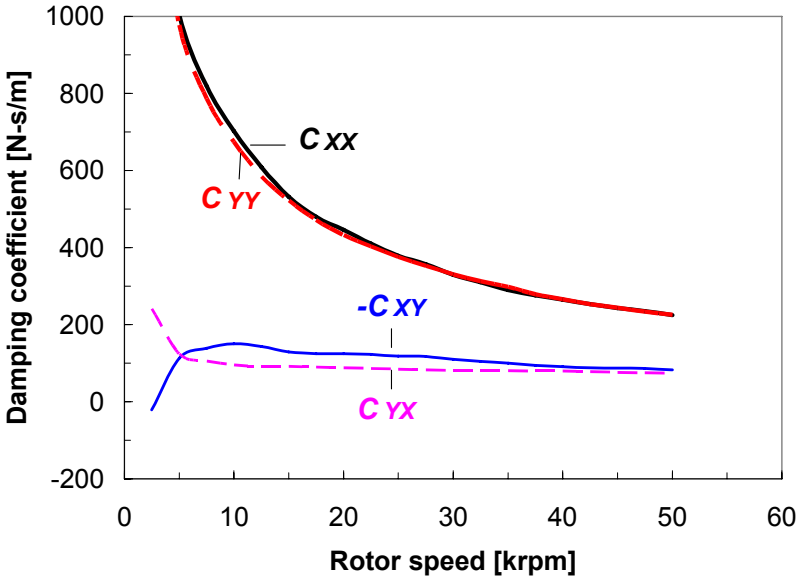

(b) Damping coefficients

Figure B2. Synchronous stiffness and damping coefficients versus rotor speed for GFBs with shims. Static load of 3.6 N in vertical (*X*) direction. Structural loss factor, γ = 0.2. Free end bearing.

APPENDIX C. COMPARISONS OF PREDICTED SYNCHRONOUS RESPONSES TO TEST MEASUREMENTS. FREE END BEARING.

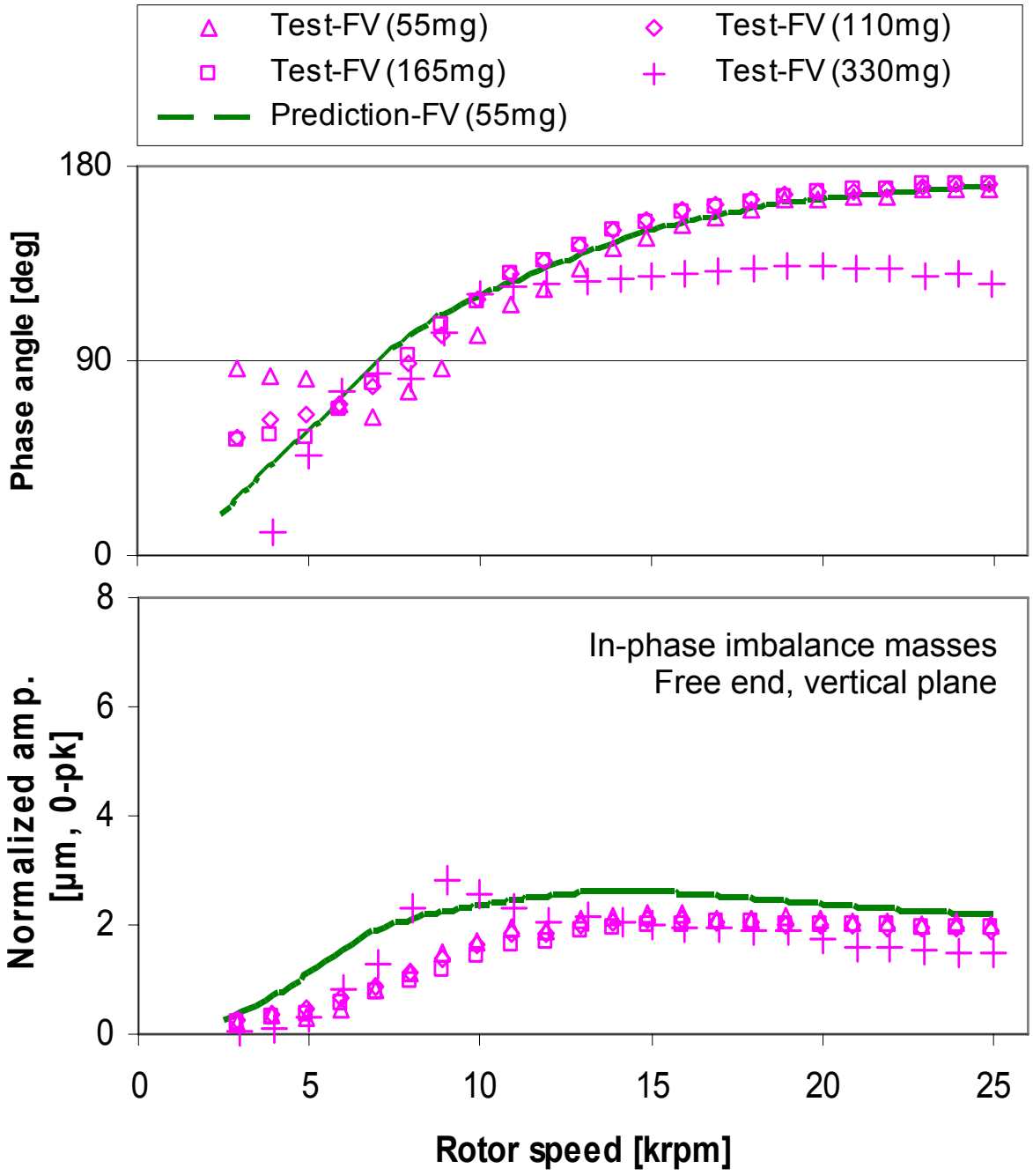

Figure C1. Phase angle and normalized rotor amplitude of synchronous response for increasing in-phase imbalance mass. Free end, vertical plane. Predictions compared to test data. Original GFBs.

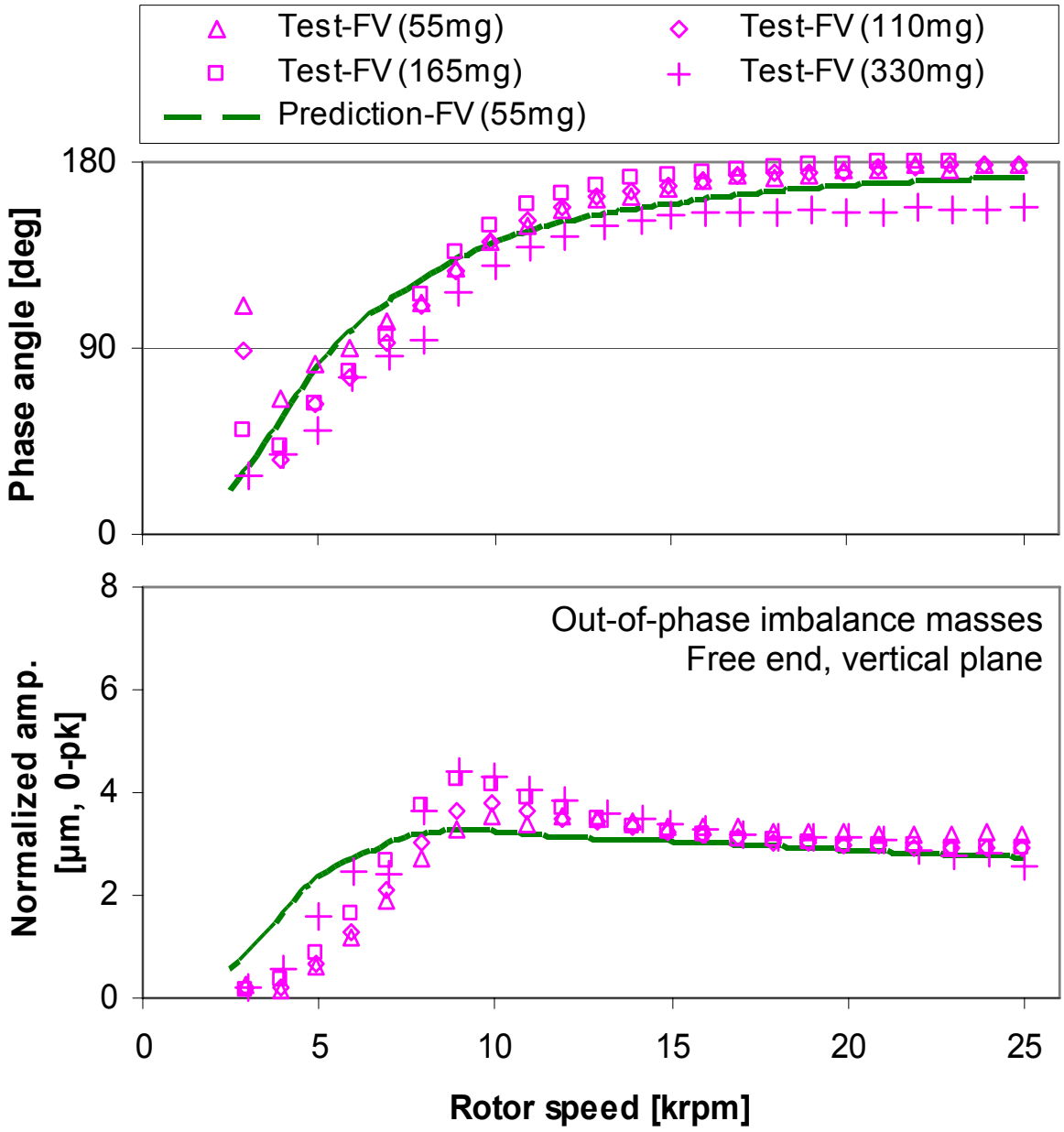

Figure C2. Phase angle and normalized rotor amplitude of synchronous response for increasing out-of-phase imbalance mass. Free end, vertical plane. Predictions compared to test data. Original GFBs.

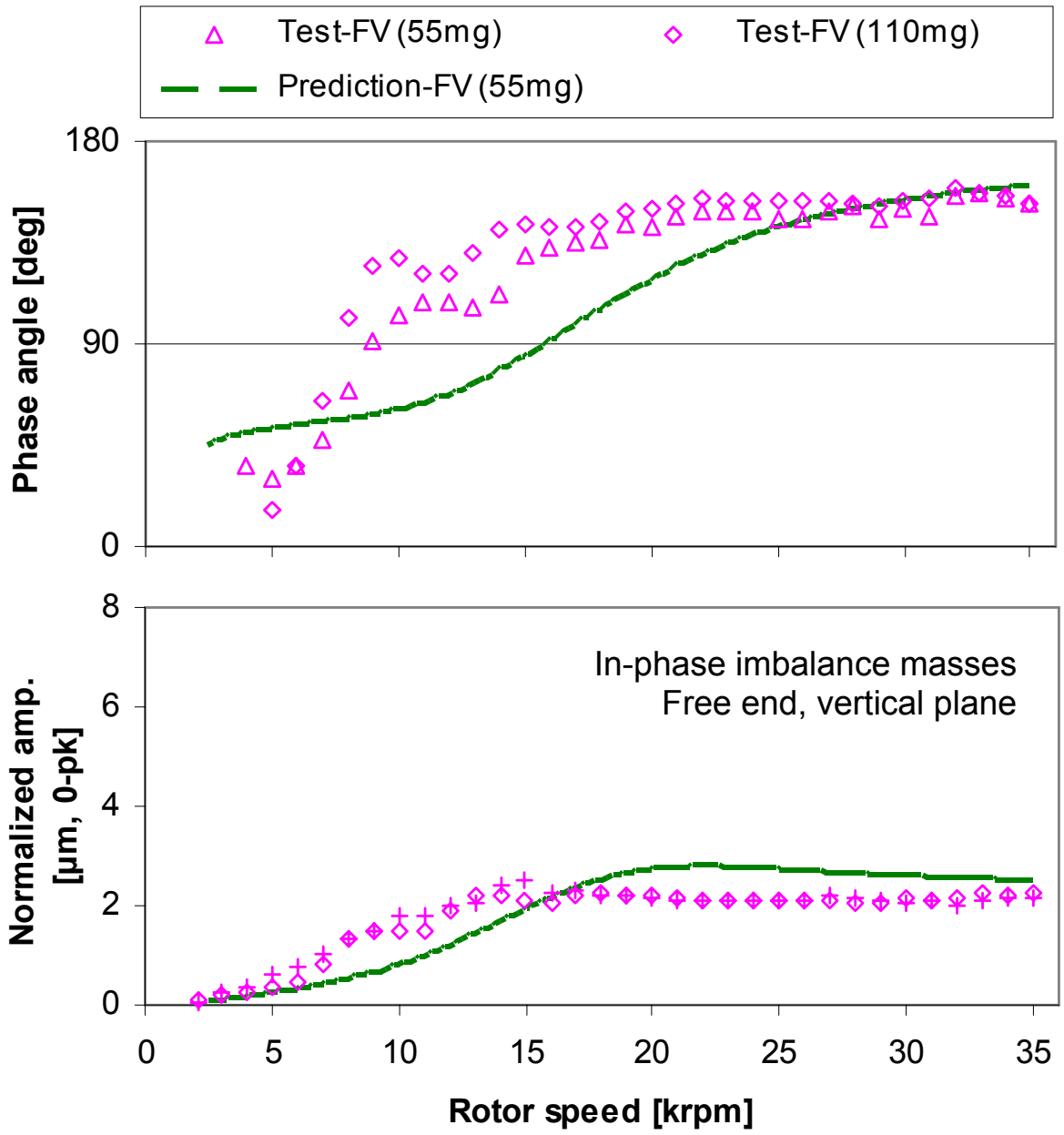

Figure C3. Phase angle and normalized rotor amplitude of synchronous response for increasing in-phase imbalance mass. Free end, vertical plane. Predictions compared to test data. Increased damping coefficients (=2×*C*'s) are used for prediction. GFBs with shims.

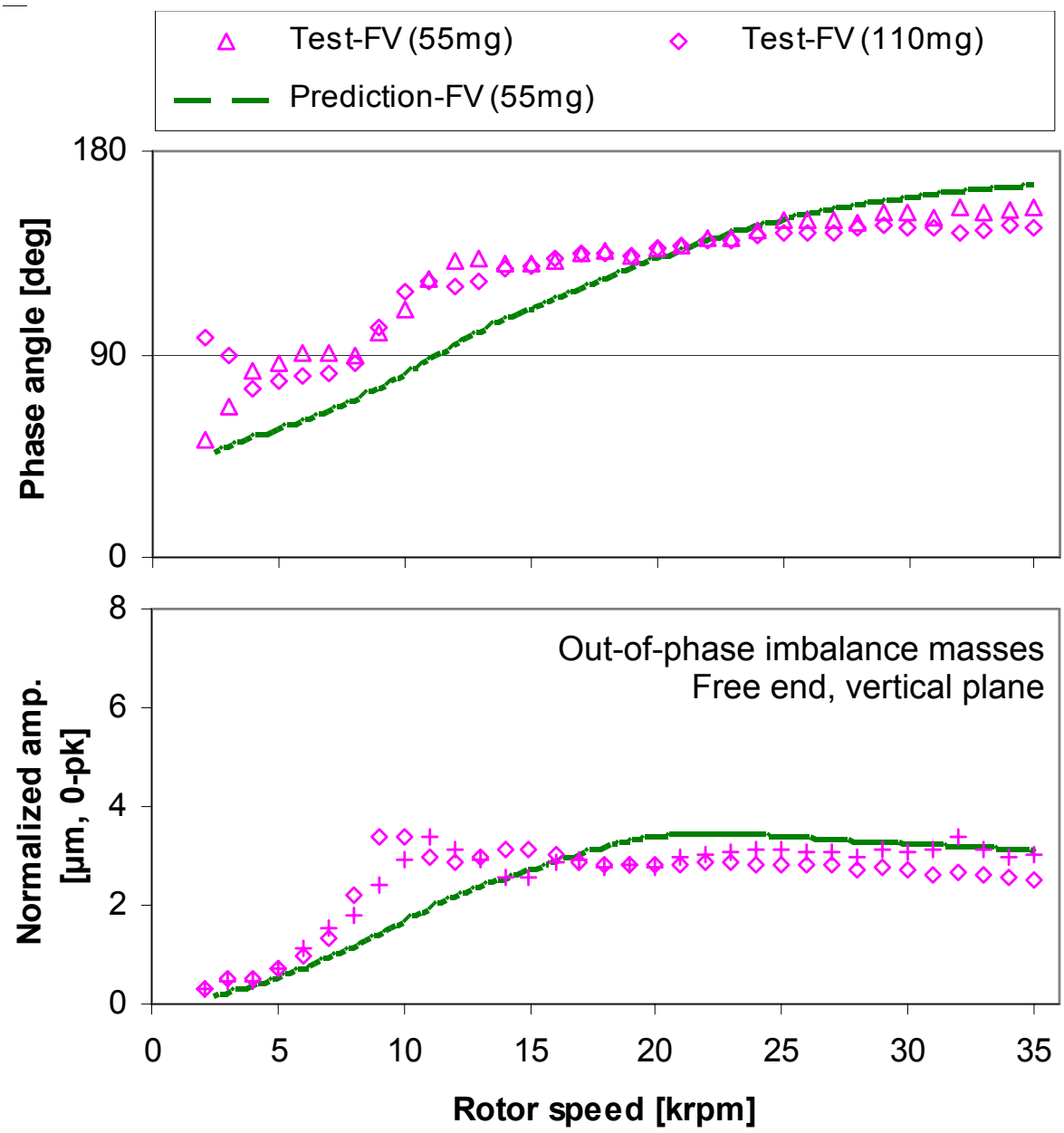

Figure C4. Phase angle and normalized rotor amplitude of synchronous response for increasing out-of-phase imbalance mass. Free end, vertical plane. Predictions compared to test data. Increased damping coefficients (=2×*C*'s) are used for prediction. GFBs with shims.